2010

Validation Of The Forebody Design Of A Ramjet-Scramjet Propulsion System Using Computational Fluid Dynamics

Jamil D. Grant
North Carolina Agricultural and Technical State University

VALIDATION OF THE FOREBODY DESIGN OF A RAMJET-SCRAMJET PROPULSION SYSTEM USING COMPUTATIONAL FLUID DYNAMICS

by

Jamil D. Grant

A dissertation submitted to the graduate faculty
in partial fulfillment of the requirements for the degree of
MASTER OF SCIENCE

Department: Mechanical Engineering
Major: Mechanical Engineering
Major Professor: Dr. Frederick Ferguson

North Carolina A&T State University
Greensboro, North Carolina
2010

School of Graduate Studies
North Carolina Agricultural and Technical State University

This is to certify that the Master's Thesis of

Jamil D. Grant

has met the thesis requirements of
North Carolina Agricultural and Technical State University

Greensboro, North Carolina
2010

Approved by:

_____	_____
Dr. Federick Ferguson Major Professor	Dr. John Kizito Committee Member
_____	_____
Dr. Messiha Saad Committee Member	Dr. Mookesh Dhanasar Committee Member
_____	_____
Dr. Samuel Owusu-Ofori Department Chairperson	Dr. Alan Letton Interim Dean of Graduate Studies

BIOGRAPHICAL SKETCH

Jamil D. Grant was born in Atlanta, Georgia on August 1, 1985. He graduated with a Bachelor of Science in Mechanical Engineering with a concentration in aerospace studies from North Carolina A&T State University in May 2007, cum laude. Prior to graduation, Mr. Grant co-authored two articles with the American Society of Mechanical Engineers.

TABLE OF CONTENTS

LIST OF FIGURES

FIGURE **PAGE**

NOMENCLATURE

A	Waverider caret angle, angle of attack
B	Shock wave angle
C_f	Skin friction coefficient
C_p	Pressure coefficient
D	Drag, force component parallel to the freestream velocity
F	Aerodynamic force
Γ	Specific heats ratio
H_∞	Flight altitude
M	Mach number
Θ	Wedge angle
P	Pressure
U	Velocity component parallel to the freestream velocity
S	Surface area
T	Temperature

ABSTRACT

Grant, Jamil D. VALIDATION OF THE FOREBODY DESIGN OF A RAMJET-SCRAMJET PROPULSION SYSTEM USING COMPUTATIONAL FLUID DYNAMICS. **(Major Advisor: Dr. Frederick Ferguson)**, North Carolina Agricultural and Technical State University.

The objective of this study is to effectively model and independently analyze the three dimensional forebody, inlet, and isolator of a conceptual Four-Point-Star Morphing Ramjet-Scramjet Engine. The analysis was conducted using computational fluid dynamic (CFD) softwares, namely, the Air Vehicle Unstructured Solver (AVUS) and FLUENT^{TM}. Ultimately a steady, three dimensional, double precision solver was used to model and analyse this very complex problem.

The morphing ramjet-scramjet engine is very unique in that, this engine actually changes its geometry to obtain optimal thrust efficiencies. This engine is capable of operating in many different propulsion regimes. The propulsion regime of interest to this study is the lower hypersonic regime. During this study, the geometry designed for a Mach 6 flowfield design was generated and analyzed to represent the propulsion regime.

FLUENT was used to conduct a 2-D viscous study. The initial result revealed that the concept developed was very promising. Results produced from the 3-D viscous analysis were inconclusive due to limitations on the computing packages. AVUS was used to conduct a 3-D viscous study. Results obtained from the 3-D inviscid study were also very promising.

CHAPTER 1

INTRODUCTION

Human development and history over the past one hundred years have been inexplicitly linked to the development of different aircraft propulsion systems. These propulsion systems operate over a wide range of propulsion régimes and are best described by the mach number scale. Typically, aircraft propulsion systems fall into three flight regimes, These are:

1) the subsonic flight regime; flight below mach 1.0,
2) the supersonic flight regime; flight between mach 1.0 and mach 5.0, and
3) the hypersonic flight regime; flight greater than mach 5.0.

Figure 1.1 below provides a brief summary of the different aircraft propulsion systems and the mach number range over which they operate. Closer examination of Figure 1.1 (William, 2005) indicates that there is only one propulsion system, which can effectively operate over the entire mach number regime; the subsonic, supersonic, and hypersonic regimes. While the objective of this research focuses on the development of an airbreathing aircraft propulsion system for the hypersonic flight regime. The author first provides a brief technical summary of the other propulsion systems and the mach number regimes over which they operate. The author looks at the rocket propulsion system, the turbojets, turbofan, and turboprops propulsion systems, the ramjet and finally the scramjets propulsion systems.

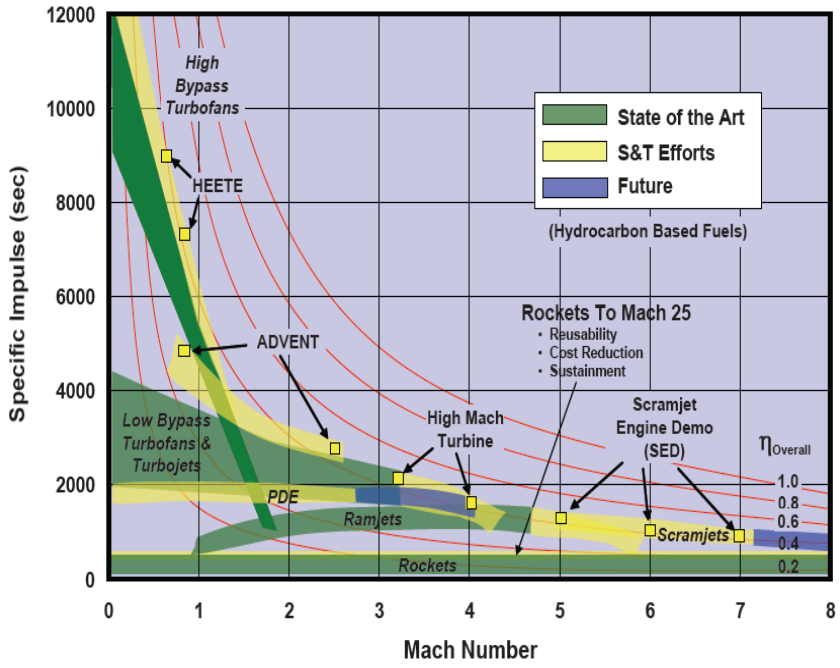

Figure 1.1. Different aircraft propulsion systems

1.1 Aircraft Propulsion Systems

It is common knowledge that all aircraft propulsion systems are founded on the basic Newtonian action-reaction principle. Figure 1.2 (Montgomerie, 2005) provides a simple chart of the various aircraft propulsion systems. Essentially, for aircraft propulsion systems air or a gas is accelerated to produce the required propulsive force. The energy used to accelerate this gas or air is obtained from the combustion of a fuel-air mixture. Fuels can be in the solid, liquid, or in vapor form. For airbreathing engines, the oxidizer required for the combustion process is obtained directly from the atmosphere. The driving force behind the design of aircraft propulsion systems is to obtain maximum engine thrust performance. Some of the jet engines that operate as airbreathing engines

include turbo-jet, trubo-prop, turbo-fan, ramjet and scramjet engines. Jet engines that carry their oxidizer supply in addition to their fuel supply are referred to as rockets.

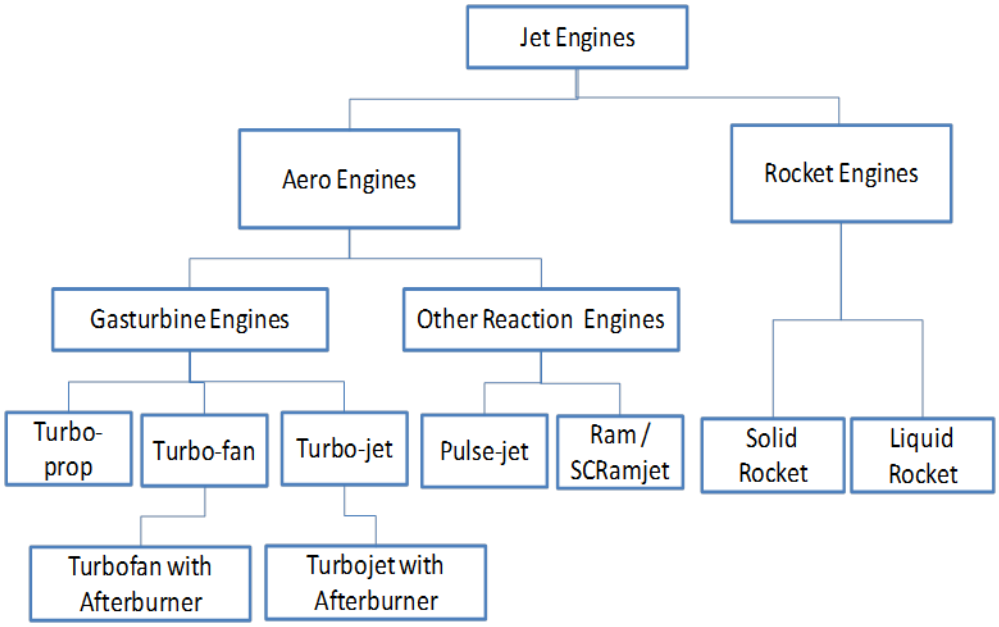

Figure 1.2. Levels of various jet engines

1.1.1 Rocket Propulsion Systems. As stated earlier, rockets are the only propulsion system that operates over the subsonic, supersonic, and hypersonic flight regimes. By design, rockets are not airbreathing aircraft propulsion systems. Rockets are designed to carry their fuel and oxidizer supplies necessary for the combustion process. Figure 1.3 (Dhanasar, 2005) presents a schematic diagram of a liquid based pump fed and a liquid based pressure fed chemical rocket. Examination of Figure 1.3 identifies the fuel

and oxidizer tanks and all the associated pumps, piping, and valves required for the rocket propulsion system to operate successfully. These auxiliary components make the rocket propulsion system large, bulky, and very complex. In terms of performance, although rockets operate over the three primary flight regimes of interest, rockets propulsion systems produce a lower specific impulse when compared against the other propulsion systems.

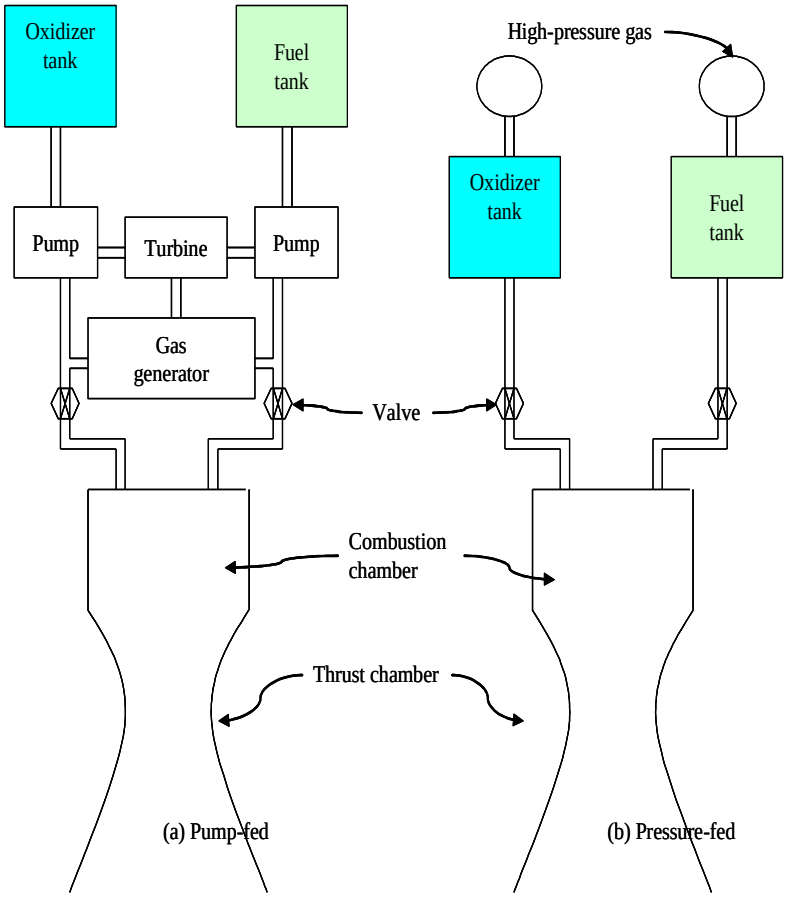

Figure 1.3. Schematic of Rocket Propulsion Systems

1.1.2 Turboprop, Turbofan, and Turbojet Propulsion Systems.

Turbo-props, turbo-fan, and turbo-jets are airbreathing engines. These propulsion systems are designed to use the oxygen in the atmosphere as the oxidizer required for the combustion process. These engines are similar to each other in that, they use a series of compressor stages to compress the incoming air before the fuel is added in the combustion process. Turbo-prop propulsion engines use gas turbines to drive a propeller in order to generate the thrust required. These engines are designed for relatively low speed vehicles which operate up to mach 0.4 (Montgomerie, 2005). Figure 1.4 (Wikipedia, 2010) presents an illustrative representation of a turbo-prop engine.

Turbo-fan propulsion engines, illustrated in Figure 1.5 (Wikipedia, 2010), are designed to operate at higher mach numbers (0.7–2.0) (Montgomerie, 2005) and can achieve velocities in the supersonic mach regime. The turbo-fan engine concept is again designed around a gas turbine engine concept. The thrust produced by a turbo-fan engine is a combination of the thrust produced by the ducted fan and the thrust produced by the exhaust gas.

Turbo-jet propulsion engines, illustrated in Figure 1.6 (Wikipedia, 2010), are also designed around the gas turbine engine concept. Turbo-jet engines operate by completing three simple steps. First, the incoming air is captured and compressed. Next, fuel is added to the compressed air to create a unique air–fuel mixture. Finally, this air-fuel mixture is burned and exhausted. It is important to note that the thrust obtained from a turbo-jet engine is a direct result of the hot exhaust gas exiting the exhaust nozzle. Turbo-jet engines are able to operate up to mach 3.0 velocities.

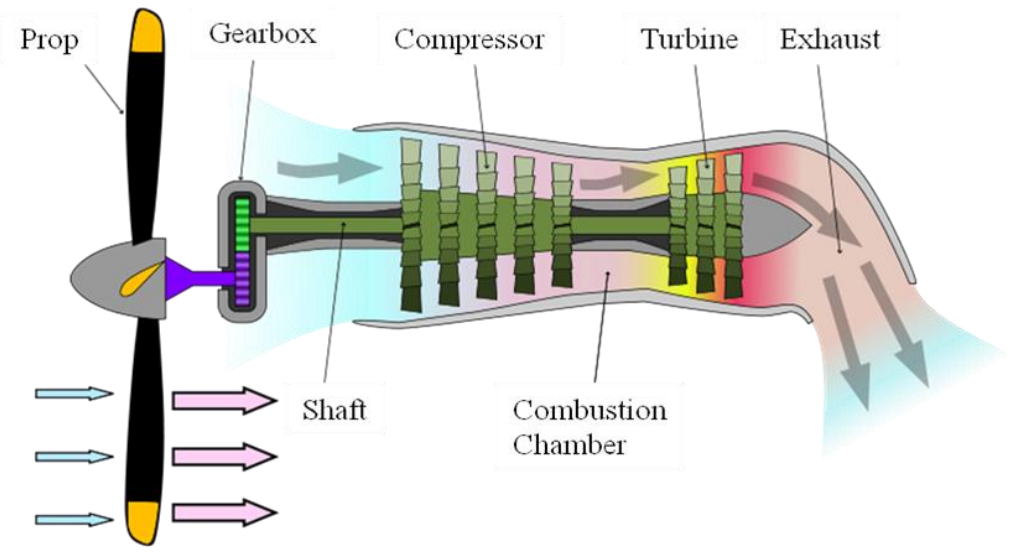

Figure 1.4. Diagram of a turbo-prop aircraft engine

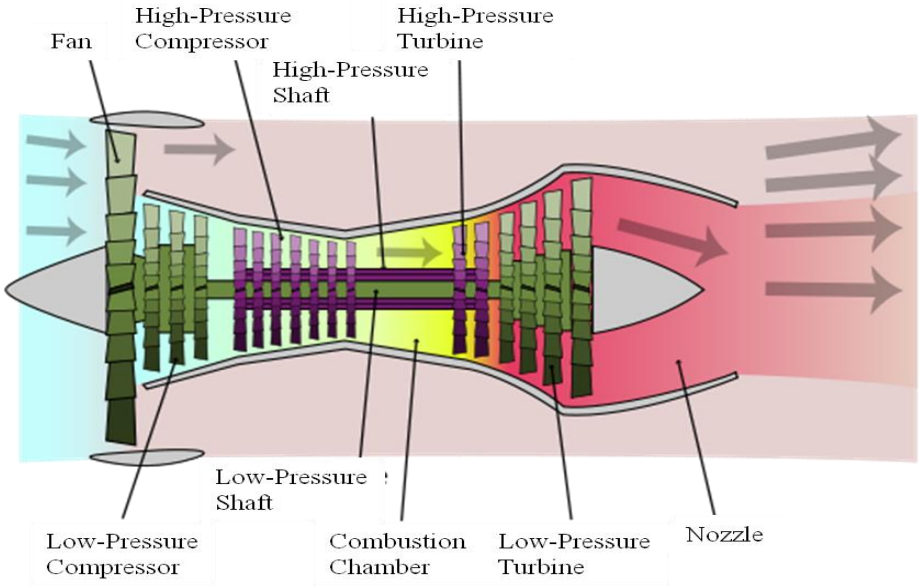

Figure 1.5. Diagram of a turbo-fan engine

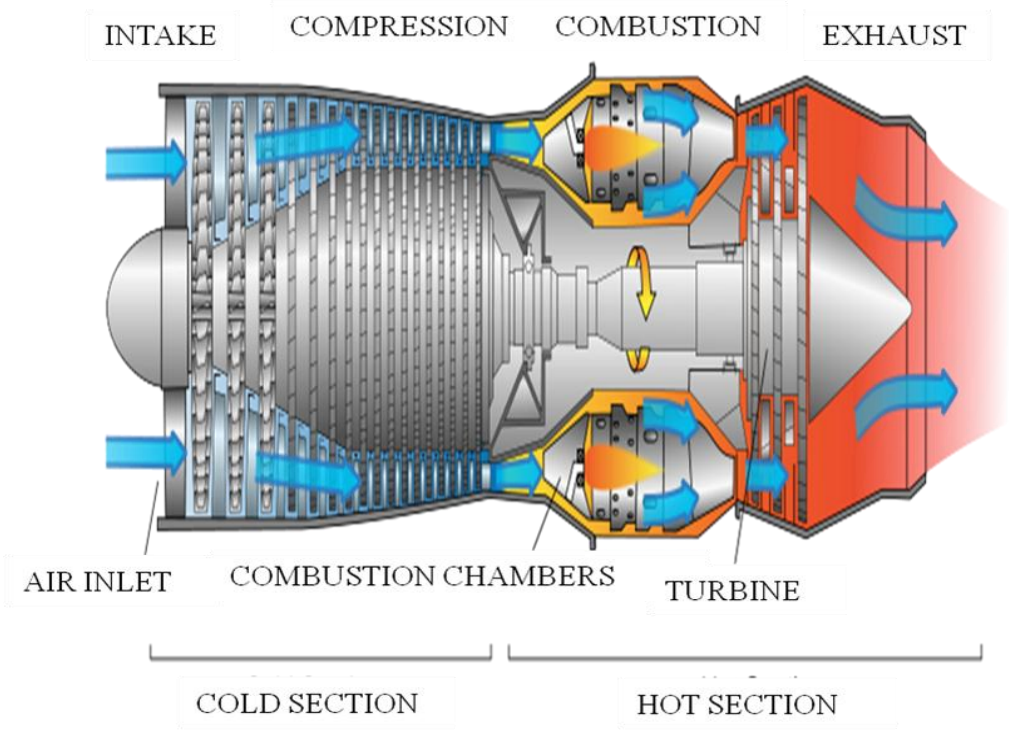

Figure 1.6. Major sections of a turbo-fan engine

1.1.3 Ramjet Propulsion Systems. A ramjet propulsion system, illustrated in Figure 1.7 (Wikipedia, 2010), represents a technology jump in the development of the jet engine concept. Ramjet propulsion systems are airbreathing engines that can only operate in a specific supersonic mach number range. This is important because ramjet propulsion systems require a shock wave to compress the incoming air. Since ramjet propulsion systems travel at supersonic velocities, combustion in a ramjet propulsion system occurs under subsonic conditions.

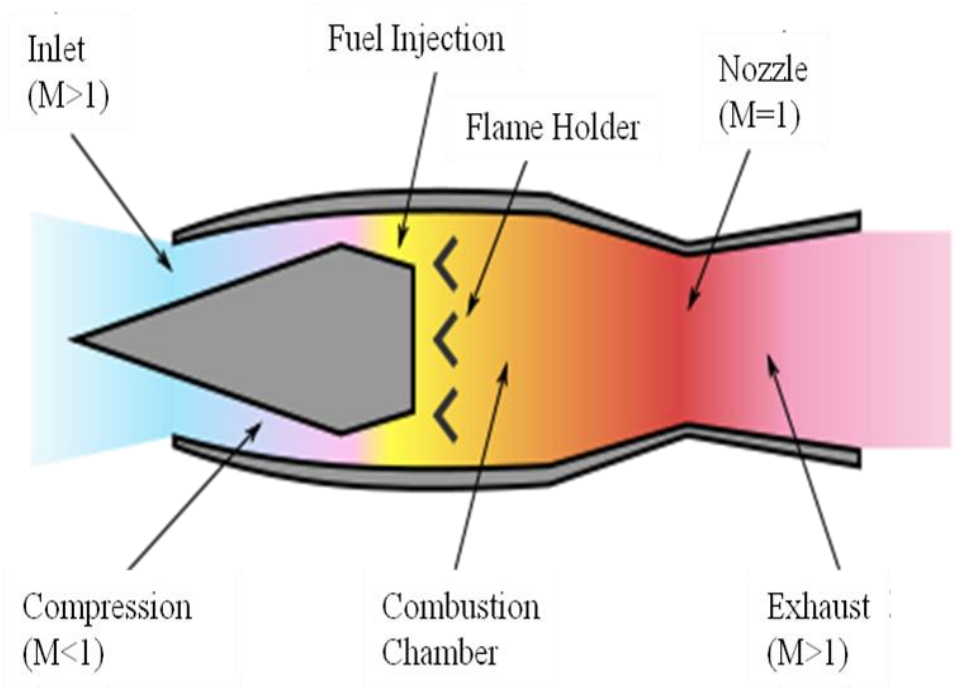

Figure 1.7. Diagram of a ramjet propulsion system

1.1.4 Scramjet Propulsion Systems. The scramjet propulsion system represents another technology jump in the development of the jet engine concept. Very similar to the operation of the ramjet propulsion systems, scramjet propulsion systems are characterized by a supersonic combustion process. Again, the incoming air is compressed by shockwaves, however fuel is added and burned in the compressed airstream while it is still traveling at supersonic velocities. The recent successful test flight of the scramjet engine concept was conducted in May 2010. The X-51 had the longest flight and achieved velocities greater than Mach 5.0 (Wikipedia, 2010). An illustrative

representation of the scramjet engine concept is presented in Figure 1.8 (Andreadis, 2005).

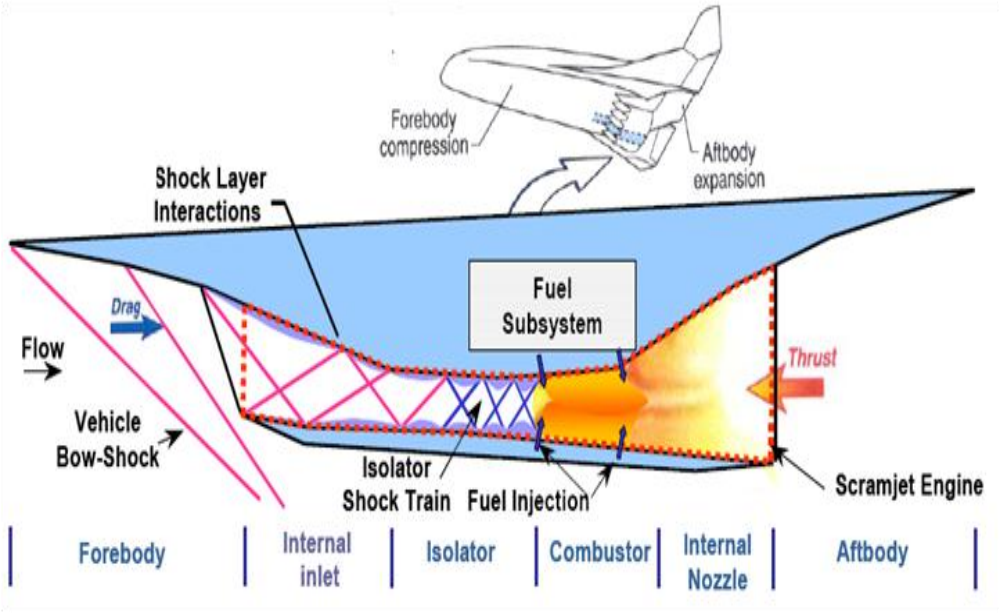

Figure 1.8. Diagram of a Scramjet propulsion system

1.2 Hypersonic Research

Aircraft propulsion systems that can propel vehicles beyond mach 5.0 are considered hypersonic propulsion systems. Most scramjet propulsion systems are considered to be hypersonic propulsion systems. The scramjet engine concept illustrated in Figure 1.8 above represents the fundamental engine design that was used in the design of the X-43A and the X-51 hypersonic vehicles that flew successfully. This design

represents a body integrated design where the scramjet engine is integrated into the airframe structure of the aircraft. Dhanasar, in his dissertation research (Dhanasar, 2009) looked into whether this design concept was practical and efficient. His research resulted in the development of a pod-mounted tip–to–tail morphing ramjet-scramjet propulsion system.

1.2.1 Need for Hypersonic Research. There has always been a long standing need to develop an aircraft propulsion system that can bridge the flight envelope existing between pure air vehicle propulsion systems and pure space vehicle propulsion systems. In the past, vehicles designed for a flight would fit into two major categories; aeronautics and astronautics. With the advancement in knowledge and technology, a new class of air vehicles is emerging. Hypersonic vehicles have the ability to bridge the gap between pure air vehicles and pure space vehicles, as is seen in Figure 1.9 (Hallion, 2005). Traditionally, aeronautic propulsion systems and astronautic propulsion systems were not integrated into one complete vehicle. The continued development of hypersonic vehicles with integrated propulsion systems will provide the thrust capabilities for aeronautic vehicles to access space.

1.2.2 Hypersonic Research at North Carolina Agricultural and Technical State University (NCAT). Hypersonic propulsion research currently conducted at North Carolina Agricultural and Technical State University stems from the work started by Dhanasar under the supervision of his academic advisor Frederick Ferguson. The work conducted by Ferguson and Dhanasar resulted in the development of a computational

model for a morphing ramjet-scramjet hypersonic propulsion system as illustrated in Figure 1.10 (Dhanasar, 2009).

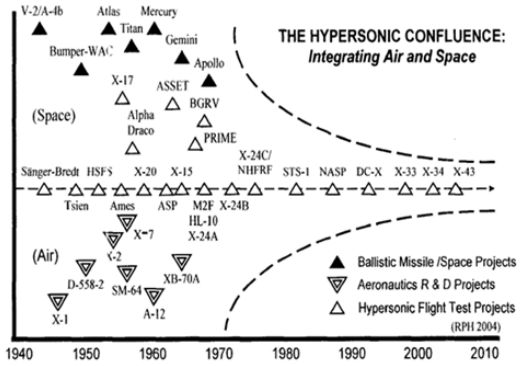

Figure 1.9. Hypersonics: The Inherent Air and Space Integrator

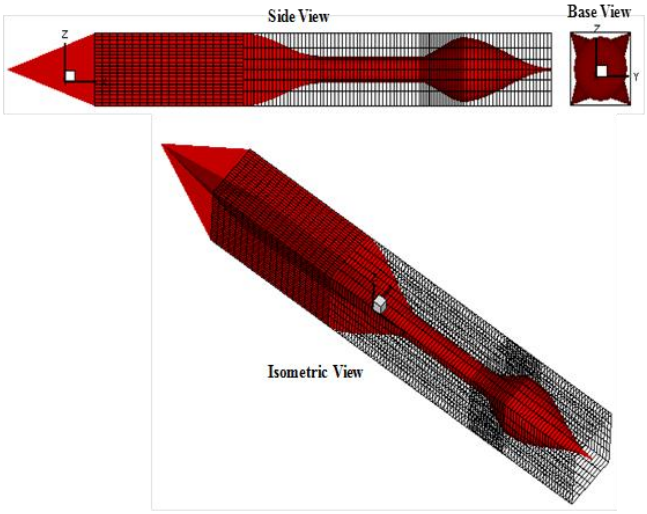

Figure 1.10. Computational Model of the Morphing Ramjet-Scramjet Engine

Conceptually the morphing ramjet-scramjet computational model was developed in three major phases. Phase one saw the development of the forebody-inlet-isolator section of the morphing ramjet-scramjet computational model. The forebody-inlet section was developed from established ideal oblique 2-D shock relationships, while the isolator section was developed from experimental correlations. Streamline cross marching techniques was then used to obtain the 3-D model for the forebody-inlet-isolator section. Information was then used from phase one to construct the transition zone-combustor-diffuser-nozzle section of the ramjet-scramjet computational model in phase two of the design process. Aerothermodynamic analysis was then conducted on phase one and a quasi-1-D chemistry model were implemented in the design of phase two. Phase three saw the integration of the geometric models and the thrust and drag analysis.

As stated earlier, one of the results obtained from the work conducted by Dhanasar was the computational model for the morphing ramjet-scramjet propulsion system, as illustrated in Figure 1.10 above. In addition to this computational model, a series of geometric design parameters were identified. An initial parametric study was conducted to determine an optimal ramjet-scramjet engine configuration. These design parameters are identified and illustrated in Figure 1.11 (Dhanasar, 2009). An aerodynamic analysis was also conducted by Dhanasar which resulted in the thrust-to-drag parameter. Figure 1.12 presents the thrust-to-drag results obtained by Dhanasar, which is plotted against the established thrust-to-drag trend.

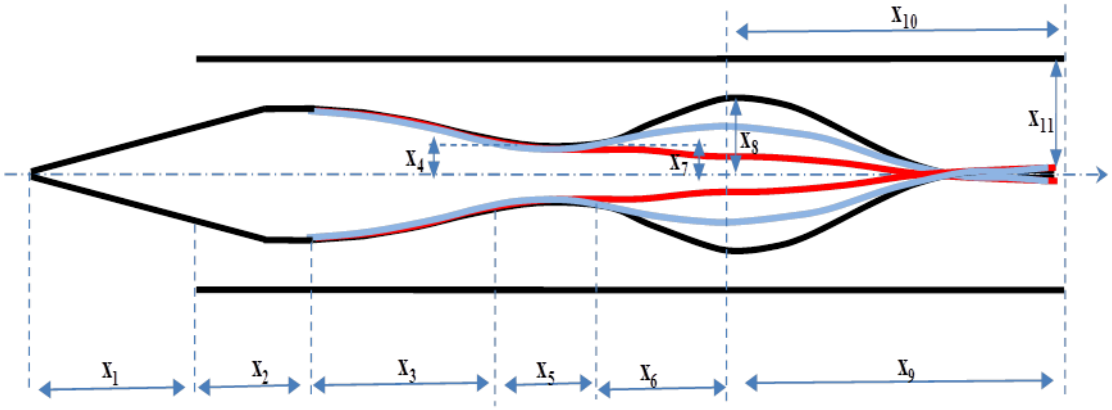

Figure 1.11. The morphing ramjet-scramjet with geometric design parameters

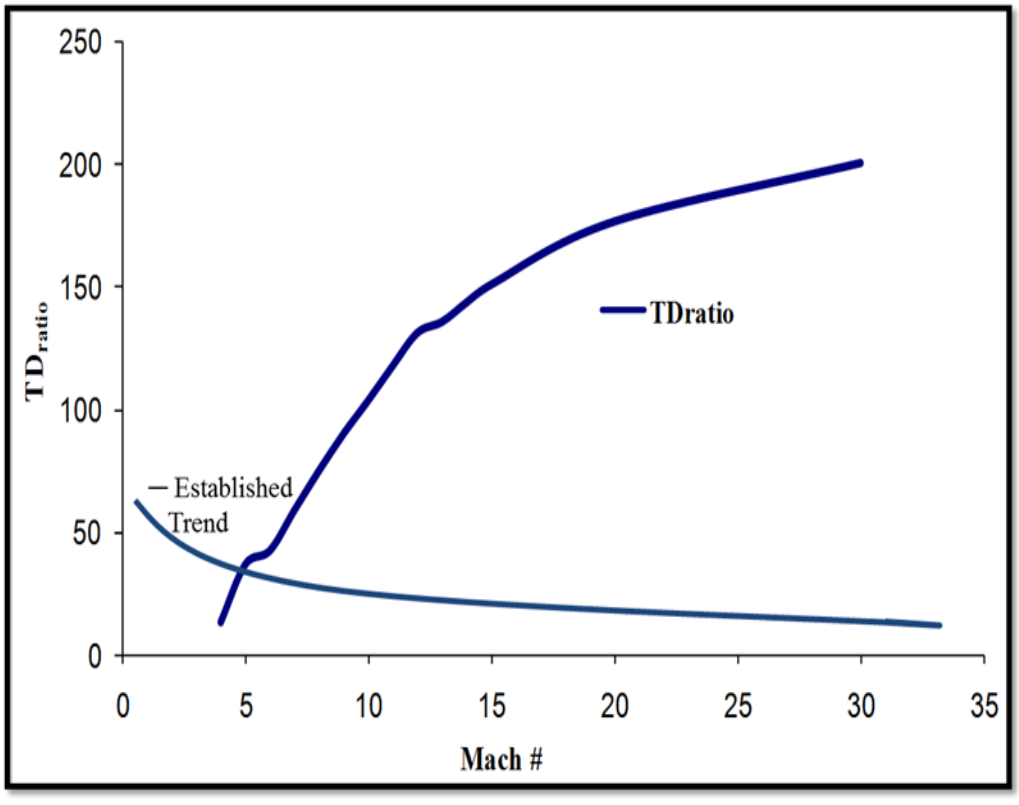

Figure 1.12. Thrust-To-Drag Results

1.3 Problem Statement

The work conducted by Dhanasar represents new information to the hypersonic community. Therefore his work needs to be independently validated. The objective of this study is to take the geometries obtained by Dhanasar's design process and to independently validate the results.

Initially, an independent viscous analysis was conducted on the forebody-inlet-isolator sections of the morphing ramjet-scramjet computational model for the four-point star configuration, as illustrated in Figure 1.13 (Dhanasar, 2009). This analysis was conducted through the use of two grid generation and computational fluid dynamic combination packages, namely, GAMBIT^{TM}-FLUENT^{TM} and Gridgen^{TM}-AVUS.

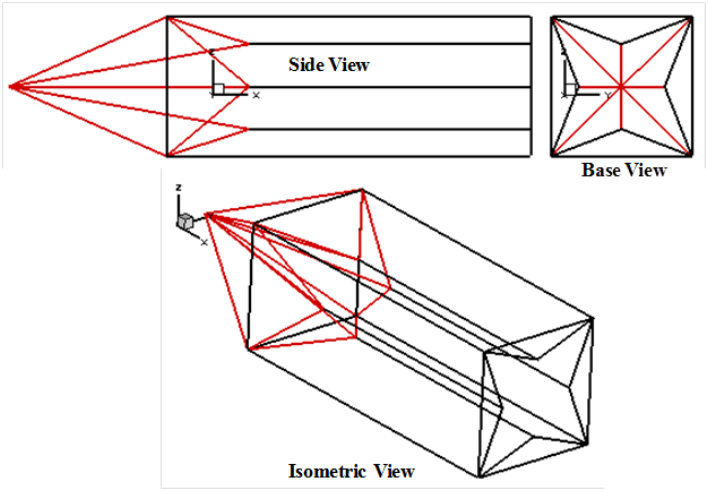

Figure 1.13. The Four-Point-Star Configuration

CHAPTER 2

HYPERSONIC DEVELOPMENTS

2.1 Inverse Design Approach to Phase I

In phase I of the design process, the centerline geometry of a given 2D scramjet configuration is explicitly constructed using the following design inputs: a Mach number, M_∞, (usually greater than 3.0), the length of the scramjet forebody, L, (a non-dimensional length of 1.0 is used as default), the shock angle, β, the caret angle, α, the cruising flight altitude, H_∞, and the isolator back-pressure ratio, P_{in}/P_{exit}. Using the Mach number and the altitude all other freestream flow parameters are computed [12-16]. The input data is used to define, construct, and analyze three important aerodynamic zones. These zones are as follows: the 'Primary Shock Zone', AB, the 'Reflected Shock Zone', BC, and the 'Isolator Zone', CD. The physics of the aerodynamics as they related to these zones are highlighted in the centerline sketch illustrated in Figure 2.1. This figure also illustrates the physics of the 2D supersonic flow as it is processed by a wedge prior to entering into a constant-area duct. The details of the aerodynamics and their exploitation in the design process are explained in the next section.

The physical derivation of the 3D 'forebody' configuration in Figure 2.1 is accomplished in two design stages. In stage one, the 2D construction of the 'forebody', domain *A-D*, is conducted, whereas, in stage two, the 2D 'forebody' model is transformed into a 3D configuration. Detail descriptions of these two design stages are provided in sub-sections 2.1.1 and 2.1.2.

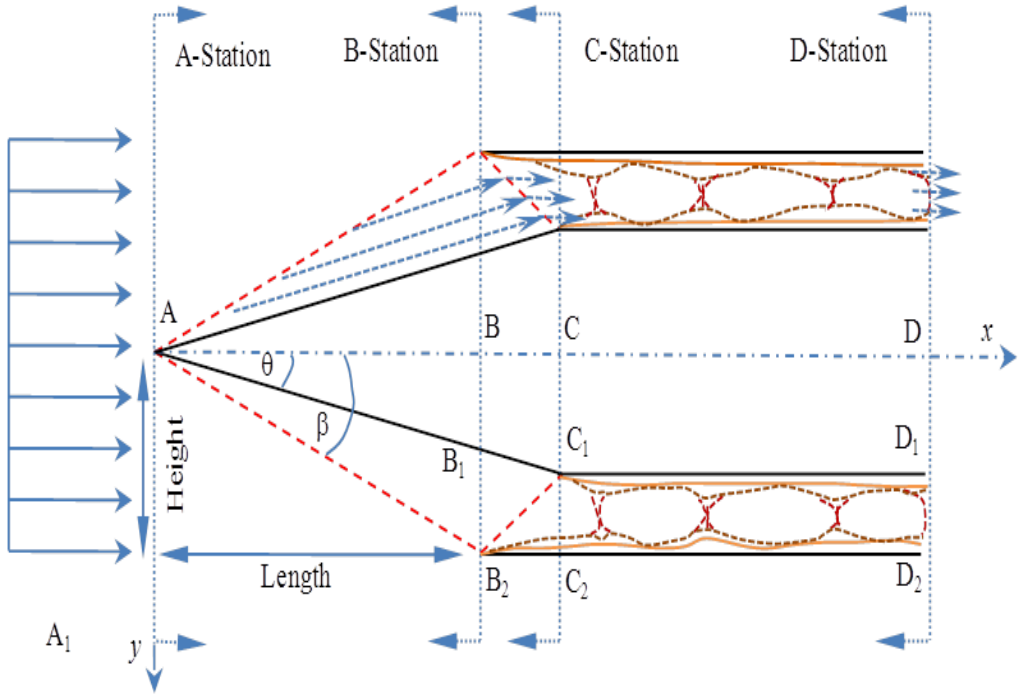

Figure 2.1. 2D cross-section of the forebody-inlet-isolator section

2.1.1 Expected Aerodynamics of the 2D forebody Configuration. Consider the aerodynamics of a supersonic flow traveling parallel to the x-axis of a 2D wedge before it is deflected twice, first by an oblique shock wave, *AB*, emanating at the leading edge, A, of the wedge, and second, by a reflected shock wave, emanating from the cowl lip, point B_2, of the inlet. Refer to the schematic illustrated in Figure 2.1. Further, consider the direction of the redirected flow. It once again travels parallel to the x-axis, but this time in an 'isolator' duct with constant cross-sectional area. If the freestream Mach number of the flow is initially chosen to be large, say a value greater than 3, and

the shock wave angle, β, chosen in the range between 12 and 30 degrees, then the flow entering the isolator duct remains supersonic.

The behavior of the flow field within the constant-area isolator is critical to the design of the dual mode scramjet, since the isolator may either be comprised of a system of normal or oblique shocks, as shown in Figure 2.2 (Dhanasar, 2009). Even though the flowfield behavior within the isolator is dictated mainly by viscous interactions, the system of normal or oblique shocks is a result of two major factors, namely, the isolator's non-dimensional length, (L/H), and the pressure conditions at the isolator outlet compared to that at its inlet. Refer to the schematic plot in Figure 2.3 (Dhanasar, 2009).

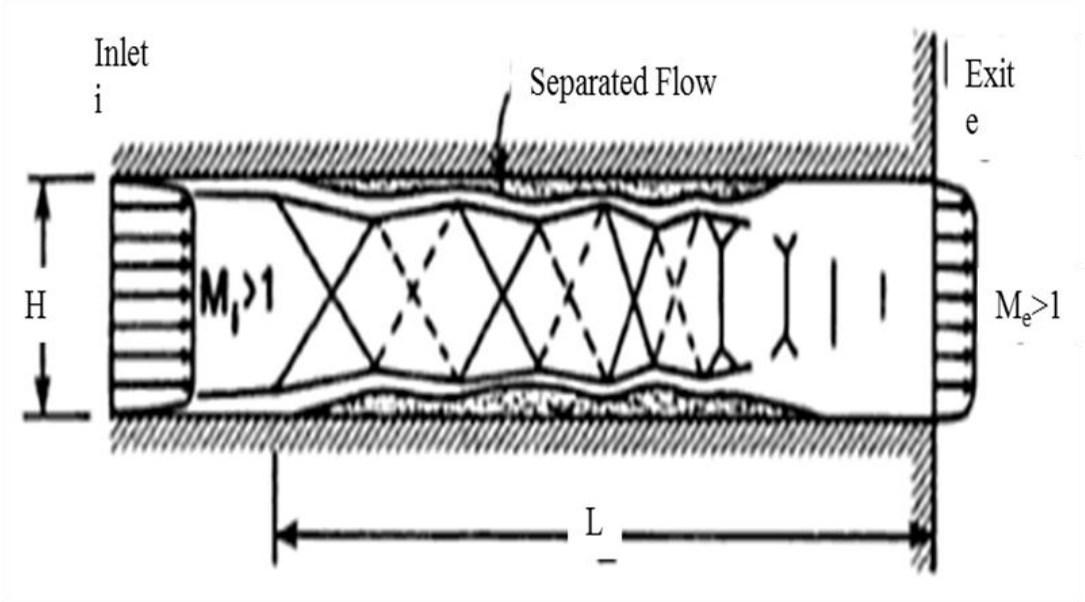

Figure 2.2. The Physics of Isolator Flows

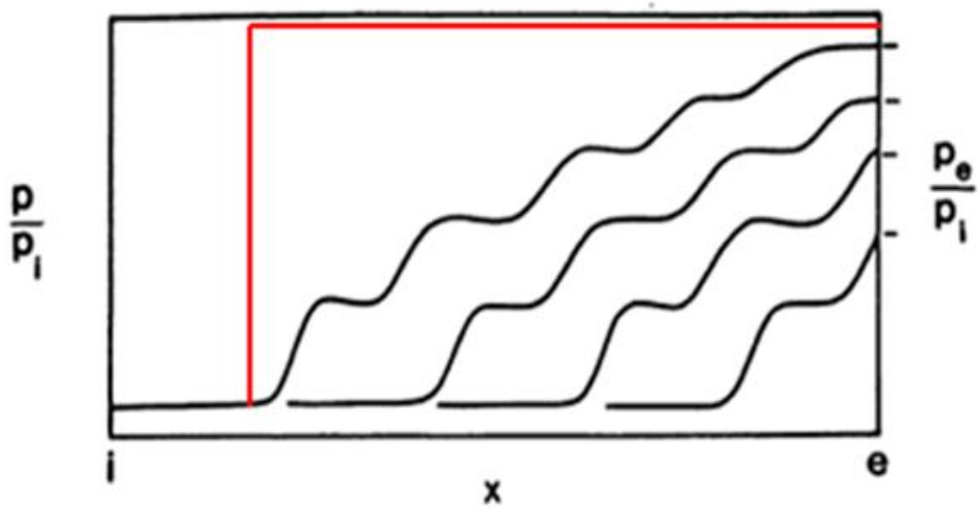

Figure 2.3. Typical Pressures within the Isolator

Referencing to Figure 2.1 again, at point D, the isolator experiences an exit static pressure, P, at point D, somewhere above the range of its inlet pressure, P_{in}, and the pressure that corresponds to a normal shock pressure at the inlet conditions, defined as $P_{n,in}$. Any 'isolator back pressure', P_{out}, greater than the pressure, $P_{n,in}$, will cause the isolator to 'unstart'. Refering again toFigure 2.3, pressures at the isolator outlet that are less than $P_{n,in}$ does not result in 'unstarts' but will either support a system of normal or a system of oblique shocks within the duct. Back-pressures closer to the upper limits will lead to the normal shock trains, whereas back pressures at the lower end of the spectrum will lead to systems of mild oblique shock trains which may occur further away from the isolator's inlet. In addition, it has been experimentally demonstrated in Waltrup and Billig, that the constant-area isolator exit pressure, P_{out}, explicitly dictates the length of the isolator. As a result, it is desirable to prescribe P_{out} such that it not only satisfies the

condition; $P_{out} \in (P_{in}, P_{n,in})$, but that it falls at the lower end of the pressure spectrum. The spectrum of P_{out}, explicitly facilitates the evaluation of the isolator's length.

2.1.2 The Derivation of the 2D "Forebody" Configuration. The 2D realization of the 'forebody' design schematically is based on the determination of important geometric points located at stations A, B C and D, along the x-axis of the scramjet. Further, the determination of these points rests on the implementation of the oblique shock relations described in Anderson and Heiser the 'isolator' relations that were experimentally derived in Waltruo and Billing. In Figure 2.1, it is assumed that the flow travels in the x-direction, and the construction of the 'forebody' configuration starts at point, *A*. In this analysis, Points A, B, C and D are located using the following explicit steps:

Point A is considered the origin of the scramjet design coordinated system, as such, point A coordinates are evaluate as follows, $A_x = 0, A_y = 0,$ and $A_z = 0$. Using the aerodynamics principles described earlier and the input data, the location of the point, B, can be computed through the use of the following relations: $B_x = L, B_y = 0,$ and $B_z = 0$.

In addition, using trigonometric relationships point B1 is evaluated as follows: $B_{1x} = L, B_{1y} = B_x \tan(\theta),$ and $B_{1,z} = 0$

Similarly, the coordinates for point B2 are evaluated as follows: $B_{2x} = L, B_{2y} = B_x \tan(\beta),$ and $B_{2,z} = 0$. The symbols, Θ and β represent the wedge and shock wave angles, respectively. Recall, the mach number and the shock wave angle are

considered ‘input data’, as such; the wedge angle Θ can be evaluated from the theta-beta-mach relation (Heiser,1994), as follows,

$$\theta = a\tan\left\{2\cot\beta\left[\frac{M_\infty^2\sin^2\beta - 1}{M_\infty^2(\gamma + \cos 2\beta) + 2}\right]\right\} \tag{2.1}$$

where the constant γ is set to 1.4.

Unlike the points at station *B*, the points at station *C* are dependent on the flow field properties behind the primary shock wave, *AB*, and the wedge angle, θ. The evaluation of the location of point C is carried out in the sequence of steps described below:

a) The Mach number, M, behind the primary shock wave, AB_2, is evaluated as follows,

$$M = \left\{\frac{1}{\sin(\beta - \theta)}\right\}\frac{\left[1 + [(\gamma-1)/2](M_\infty \sin(\beta))^2\right]}{\left[\gamma(M_\infty \sin(\beta))^2 - (\gamma-1)/2\right]} \tag{2.2}$$

b) With the mach number behind the primary shock wave AB_2 known, and the free stream parameters given, the oblique shock relations derived in Anderson are used to evaluate all flow field properties behind the primary shock. The, pressure, P, temperature, T, densities, ρ, and total pressure, $P_{t,2}$, can be determined using Equations (2.3) to (2.7).

$$\frac{P}{P_\infty} = \frac{2\gamma\left(M_\infty \sin\beta\right)^2 - \left(\gamma - 1\right)}{\left(\gamma + 1\right)} \tag{2.3}$$

$$\frac{T}{T_\infty} = \frac{\left[2\gamma\left(M_\infty \sin\beta\right)^2 - \left(\gamma - 1\right)\right]\left[\left(\gamma + 1\right)\left(M_\infty \sin\beta\right)^2 + 2\right]}{\left(\gamma + 1\right)^2\left(M_\infty \sin\beta\right)^2} \tag{2.4}$$

$$\frac{\rho}{\rho_\infty} = \left[\frac{\left(\gamma + 1\right)\left(M_\infty \sin\beta\right)^2}{\left(\gamma + 1\right)\left(M_\infty \sin\beta\right)^2 + 2}\right] \tag{2.5}$$

$$\frac{P_{t,2}}{P_{t,\infty}} = \left[\frac{\left(\gamma + 1\right)\left(M_\infty \sin\beta\right)^2}{\left(\gamma + 1\right)\left(M_\infty \sin\beta\right)^2 + 2}\right]^{\frac{\gamma}{\gamma-1}}\left[\frac{\left(\gamma + 1\right)}{2\gamma\left(M_\infty \sin\beta\right)^2 - \left(\gamma - 1\right)}\right] \tag{2.6}$$

c) The reflection shock wave, B_2C, occurs as a result of the supersonic flowfield with mach number, M, behind shock wave, AB_2, being deflected once again by a second 'imaginary' wedge originating at point B_2 with an angle θ. This second 'imaginary' wedge is aligned such that the resulting deflected flow travels parallel to the x-axis. The values of the new parameters, M and θ, are computed using Equations (2.1) and (2.2). Further, the reflection shock angle, ϕ, can be expressed as: $\phi = \beta_1 - \theta$, where the symbol, β_1, represents the reflected shock angle generated by the 'imaginary' wedge of angle θ as it interacts with the flow field of mach number, M. The value for β_1 can be computed by solving Equation (2.1) iteratively while replacing the value of M_∞ with that of M.

d) In a similar manner, the Mach number, M1, behind the reflected shock can be obtained from Equation (2. 2) by replacing the value of M∞ with that of M, and the value of β with β1. The mach number value, M1, also represents the entrance mach number of the flow field to the isolator duct. Again, using the oblique shock

relations, Equations (2.3) to (2.6), the flow field properties, p_1, T_1, ρ_1 and T_o, are determined.

e) Now that the parameters, θ, β and β_1 are determined, points at station C can be evaluated. Using the trigonometric relations illustrated in Figure 2.1, the coordinates, C_x, C_y and C_z, are computed as follows:

$$C_x = \left[1 + \frac{\tan(\beta) - \tan(\theta)}{\tan(\theta) - \tan(\beta_1 - \theta)}\right] B_x \tag{2.7}$$

While $C_y = 0$ and $C_z = 0$

f) The coordinates of point C_1 are determined as follows: $C_{1x} = C_x, C_{1y} = C_x \tan(\theta)$, and $C_{1,z} = 0$

g) Similarly, the coordinates of point C2 are determined from: $C_{2x} = C_x, C_{2y} = B_{2y}$, and $C_{2,z} = 0$

In a process similar to the one described in the determination of points at station *C*, the evaluation of the point at station *D* is accomplish through the execution of the following steps:

a) Using the Mach Number, M_1, and the static pressure, P_1, as the entrance Mach number, M_{in}, and pressure, P_{in}, to the isolator, the equivalent non-dimensional 'normal total' pressure value, $P_{n,in}$, based on the entrance conditions can be determined as follows:

$$\frac{P_{n,in}}{P_{in}} = \left[\frac{2\gamma M_1^2 - (\gamma - 1)}{(\gamma + 1)}\right] \tag{2.8}$$

As described earlier, an appropriate value representing the ratio of the entrance and exit pressures, P_{in}/P_{out}, in the range between P_{in} and $P_{n,in}$ must be evaluated. This value is needed in order to determine the length of an isolator that can reliably prevent all 'unstart' conditions. In this analysis, however, the ratio, $P_{out}/P_{n,in}$, representing the isolator exit pressure, P_{out}, to the 'normal total' pressure value, $P_{n,in}$, is prescribed. Using this approach, the value for P_{in}/P_{out} can be determined as follows:

$$\frac{P_{out}}{P_{in}} = \left(\frac{P_{out}}{P_{n,in}}\right)\left(\frac{P_{n,in}}{P_{in}}\right) \tag{2.9}$$

b) The system of 1D conservation laws result in the following expression for the isolator exit mach number, M_{out} ;

$$M_{out} = \left\{ \frac{\gamma^2 M_{in}^2\left[1+\left((\gamma-1)/2\right)M_{in}^2\right]}{\left(1-\gamma M_{in}^2 - P_{out}/P_{in}\right)^2} - \left(\frac{\gamma-1}{2}\right) \right\}^{\frac{1}{2}} \tag{2.10}$$

Similarly, with the exit mach number known, the non-dimensional length of the isolator can be evaluated based on the following experimental relationship developed in Waltrup and Billig:

$$\left(\frac{L}{H}\right)_{Isolator} = \frac{\sqrt{\theta/H}}{\left(\mathrm{Re}_\theta\right)^{\frac{1}{4}}} \frac{\left\{50\left(\left(P_{out}/P_{in}\right)+1\right)+170\left(\left(P_{out}/P_{in}\right)-1\right)^2\right\}}{M_{in}^2-1} \tag{2.11}$$

where Re_θ is the inlet Reynolds number based on the momentum thickness. Also, the symbol, *H*, represents the isolator height that is determined from the y-coordinates of points C_2 and C_1, such that, $H = C_{2y} - C_{1y}$.

c) The coordinates of point D are computed as follows: $D_x = C_x + L_{Isolator}$, $D_y = 0$ and $D_z = 0$.

d) The coordinates of point D_1 are computed as follows: $D_{1x} = D_x$, $D_{1y} = C_{1y}$ and $D_{1z} = 0$.

e) The coordinates of point D_2 are computed as follows: $D_{2x} = D_x$, $D_{2y} = C_{2y}$ and $D_{2z} = 0$.

f) Finally, with the coordinates of all points at all stations, A, B, B_1, B_2, C, C_1, C_2, D, D_1, and D_2, fully defined, the sketch illustrated in Figure 2.1 can be accomplished.

2.1.3 Extension of the 2D Model to the 3D Scramjet Forebody Configurations. The transformation of the 2D configuration illustrated in Figure 2.1 into a 3D configuration that preserves the 2D nature of the flowfield starts with transforming one section at a time. To illustrate the 3D transformation process, the Forebody-Inlet-Isolator configuration sketched in Figure 2.1 is separated into its three distinct sections, through the use of common interfaces or stations, namely, A-, B-, C- and D-Stations. Please refer to Figure 2.1. Attempts are made to illustrate the transformation of each section into its 3D counterpart. As each section is transformed into its respective 3D counterpart, the 2D nature of the flowfield is also preserved.

The transformation process used in this analysis is based on an inverse design approach, the so-called waverider design approach that was first suggested by Terrence Nonweiler (Billig,1993) in 1959. Even though, the Nonweiler's waverider approach

(Ferguson, 2007) of inversely carving stream surfaces from inviscid flowfields is well documented , a brief description of this process is warranted. This description is provided in Appendix A.

2.1.4 Streamtube Construction Using the Waverider Approach. In this analysis, an alternative view point on the design of waveriders is proposed. Here, the focus not only of the waverider shape, but also on the external flow field supporting the configuration. In reference to Figure 2.1, the focus is on the external flow below the waverider lower surfaces, AB_1H and AB_2H, and the flow entering and exiting the planes, HB_1B_2 and HB_1B_2. Using this alternative perspective, the flow traversing the lower surface of the waverider can be viewed as the flow entering a stream tube through the surface, AB_1B_2 and leaving through the plane, HB_1B_2. In this case, the flow within the stream tube is bounded by the lower inviscid surfaces, AB_1H and AB_2H and an imaginary line surface, B_1B_2. In addition, the flow field within this tube is strictly two dimensional, and is assumed to be confined only to the XY-plane. This alternative point of view is further expanded to include the combination of multiple stream tubes, the surfaces of which are constructed from 2D flow fields. The challenge is therefore to identify methods that allows for the evaluation of the 'waverider design points' and their use in the generation of inviscid flow fields, stream surfaces, stream tubes and waverider configurations that support the resulting flow fields.

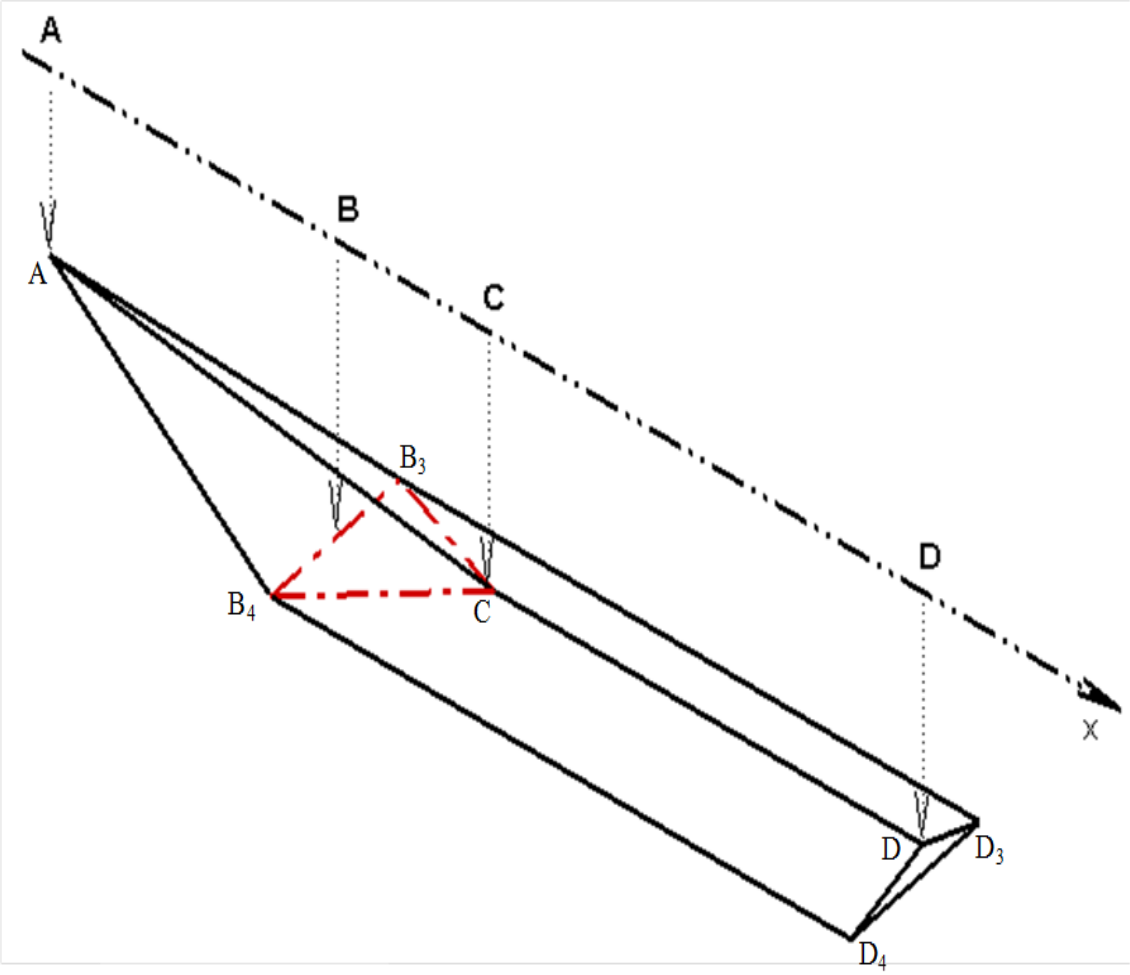

Figure 2.4. Waverider Derived Stream Tube

Consider the waverider derived stream tube illustrated in Figure 2.4. The challenge is to now demonstrate that this stream tube was derived from a supersonic flowfield that started out travelling parallel to the x-axis, gets compressed by two specially constructed oblique shock waves, and ends up travelling once again parallel to the x-axis. During the construction a typical stream tube, it is important to note that the

focus is always on the flowfield, while the inviscid stream surface containing the flow is comprised of the streamlines that travels along the boundaries of the specified flowfield.

With the waverider construction philosophy described in the previous sections in mind, consider a 2D flowfield that is initially travelling parallel to the x-axis. Now, consider that this flow as it encounters a primary oblique shock plane, say plane AB_3B_4, as illustrated in Figure 2.4. According to the waverider design concept, the primary shock wave plane, AB_3B_4, will support the compression surfaces, ACB_3 and ACB_4, as the flow field is deflected. Of course, the deflected flow no longer travels parallel to the x-axis. Now, imagine that a reflected shock wave is specially constructed to form the plane, CB_3B_4, which is designed to straighten the flow leaving the shock surface, CB_3B_4, so that it once again is on a path parallel to the x-axis. The reflected flow now forms the stream tube comprising of the following planar surfaces, CDD_3B_3, CDD_4B_4, and $B_3B_4D_4B_3$.

In summary, the stream tube illustrated in Figure 2.4, is made up of seven points, namely points; A, B_3, B_4, B, C, D_3, D_4, and D. Recall, the evaluation of these points were described earlier in this analysis. Using the philosophical design approach described above, the stream tube illustrated in Figure 2.4 is derived such that the inviscid flow is truly two dimensional and all its aerodynamics features fully preserved. By taking this design concept one step further, four stream tubes can be pieced together to form scramjet inlets similar to the one illustrated in Figure 2.5 (Dhanasar, 2009).

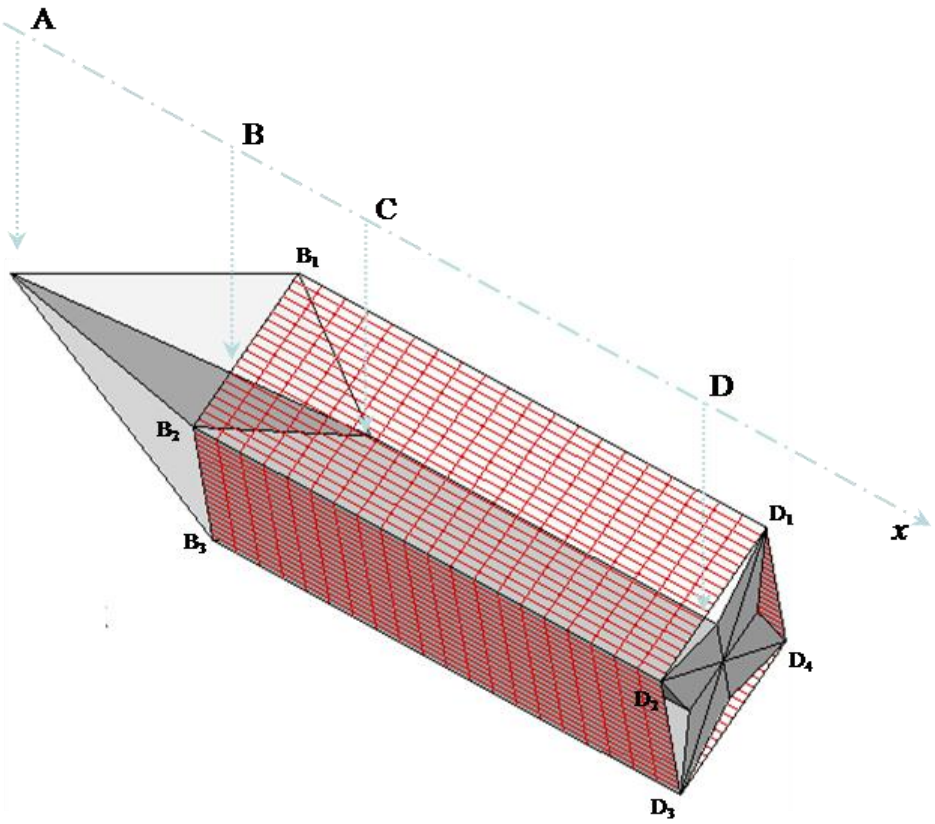

Figure 2.5. A 4-Points Star-Shaped Scramjet Forebody

An important step in this design process is the realization of stream tubes which can be used in combination to generate 'closed formed' configurations of interest to the aircraft and missile design communities. The key to transforming the 2D configuration illustrated in Figure 2.1 into its 3D counterpart illustrated in Figures A1.2 and A1.3 is based mainly on identifying the coordinates in the z-axis. In this case, the identification of points, B_3, B_3, D_3 and D_4, is of paramount importance. First and foremost, the points B_3, B_4, D_3 and D_4, are developed such that the resulting configuration forms a closed tube

that preserve the aerodynamic of the inviscid flow field described earlier. Secondly, the y and z coordinates of points, B_3, B_4, C, D_3 and D_4, are dependent of the choice of angle α, (ie., angle D_3DD_4), refer to Figure A1.1. In the case on a four pointed star-shaped configuration the angle α is set to 90 degree.

CHAPTER 3

THE CFD EVALUATION PROCESS

3.1 The CFD Design Process

In general, any Computational Fluid Dynamics (CFD) process starts with two sets of software packages (Elamin, 2008). A set of Pre and Posting Processing (PPP) Tools, such as Gridgen™ or GAMBIT™, and a Navier-Stokes (NS) Solver, such as, USM3d, FLUENT™ or AVUS. The NS solver consists of a numerical representation of the system of conservation laws and an arbitrary set of boundary and initial conditions. In addition, the NS solver is designed to accept information that represents arbitrary geometries and arbitrary flowfield domains surrounding those geometries. The PPP tools are designed to provide three major functions. First, they are designed to create arbitrary geometries and flowfield domains that are compatible with the requirements of a wide variety of NS solvers. Second, they are designed to provide a compatible set of grids (or computational nodes) to the NS Solver. Finally, PPP tools are designed to provide the required boundary conditions under which the flowfield solutions are to be provided (Elamin, 2008).

It is of interest to note that these tools are of two major types; namely Commercial and Research types. The Commercial based CFD tools, such as GAMBIT and FLUENT, are usually designed with sophisticated Graphical Users' Interfaces (GUIs) and does not allow for the independent manipulation of the software code. Also, in most cases, they are designed to provide a converged solution to the NS solver at each grid point

irrespective to their degree of accuracy. On the other hand, the Research based NS Solvers allow for maximum manipulation of the NS solver code. More importantly, Research based NS Solvers provide a very high degree of accuracy in their final solutions to the flowfields of interest when converged solution are possible. Experience has shown that Research based NS Solvers do not always converge, as they are very sensitive to the grids and their arrangements. The major drawback of the Research based NS solvers is the fact that they are relatively not easy to use, and an advanced knowledge of fluid dynamics is its major requirement (Elamin, 2008).

In an effort to technically support the ongoing scramjet design and research efforts at North Carolina A&T State University (NCAT), a detailed and independent CFD analysis of one of its designs is conducted. This analysis is facilitated through the use both Commercial and Research based CFD tools. The two sets of CFD tools of interest to this analysis are: 1) The FLUENT-GAMBIT combination available at NCAT and 2) the AVUS^{TM}-Gridgen^{TM} combination available at AFRL-WPAB. These codes are extremely important to the current thesis, and their descriptions are warranted. In the next two sections brief descriptions of the NS Solvers and the PPP tools are provided.

3.2 The Navier-stokes Solver

Of interest to this analysis are two NS solvers; namely, FLUENT and AVUS. However, common to both of these tools and of significant interest to this study, is the system of NS equations and the appropriate fluid dynamic models that these tools are build upon. The Navier-Stokes equations are described herein.

The typical NS Solver consists of a set of the conservation of mass, momentum and energy equations in either differential or the integral form (Elamin, 2008). Coupled to the NS equations are auxiliary equations, which represent the fluid models of interest, for example, compressible or incompressible flows, Newtonian or Non-Newtonian flows, and laminar or turbulent flows. A typical set of NS equations (Conservation of Mass, Momentum, and Energy respectfully) in the differential form found in CFD solvers are as follows:

$$\frac{\partial \rho}{\partial t} + \nabla\left(\rho \bar{V}\right) = 0 \tag{3.1}$$

$$\frac{\partial (\rho u)}{\partial t} + \nabla\left(\rho u \bar{V}\right) = -\frac{\partial p}{\partial x} + \frac{\partial \tau_{xx}}{\partial x} + \frac{\partial \tau_{xy}}{\partial y} + \frac{\partial \tau_{xz}}{\partial z} \tag{3.2}$$

$$\frac{\partial (\rho v)}{\partial t} + \nabla\left(\rho v \bar{V}\right) = -\frac{\partial p}{\partial x} + \frac{\partial \tau_{yx}}{\partial x} + \frac{\partial \tau_{yy}}{\partial y} + \frac{\partial \tau_{yz}}{\partial z} \tag{3.3}$$

$$\frac{\partial (\rho w)}{\partial t} + \nabla\left(\rho w \bar{V}\right) = -\frac{\partial p}{\partial x} + \frac{\partial \tau_{zx}}{\partial x} + \frac{\partial \tau_{zy}}{\partial y} + \frac{\partial \tau_{zz}}{\partial z} \tag{3.4}$$

$$\begin{aligned} \frac{\partial}{\partial t}\left[\rho\left(e + \frac{V^2}{2}\right)\right] + \nabla\left[\rho\left(e + \frac{V^2}{2}\right)\bar{V}\right] &= -\frac{\partial (up)}{\partial x} - \frac{\partial (vp)}{\partial y} - \frac{\partial (wp)}{\partial z} \\ &+ \frac{\partial (u\tau_{xx})}{\partial x} + \frac{\partial (u\tau_{yx})}{\partial y} + \frac{\partial (u\tau_{zx})}{\partial z} + \frac{\partial (v\tau_{yx})}{\partial x} + \frac{\partial (v\tau_{yy})}{\partial y} + \frac{\partial (v\tau_{yz})}{\partial z} \\ &+ \frac{\partial (w\tau_{zx})}{\partial x} + \frac{\partial (w\tau_{zy})}{\partial y} + \frac{\partial (w\tau_{zz})}{\partial z} + \frac{\partial}{\partial x}\left(\dot{q}_x\right) + \frac{\partial}{\partial y}\left(\dot{q}_y\right) + \frac{\partial}{\partial z}\left(\dot{q}_z\right) \end{aligned} \tag{3.5}$$

In Equations (3.1 to 3.5), the symbols, ρ, u, v, w, T, and p represent the density, the x, y and z-velocity components, temperature and pressure. The symbols, t, x, y and z, represent the independent flowfield variables. These variables are used to describe the

flowfield domain, and provide a placeholder for the unique solution. Traditionally, fluid velocity, $\bar{V}$, and heat flux, $\dot{q}$, are described through the use of the following vector quantities,

$$\bar{V} = u\,\bar{i} + \quad v\,\bar{j} + \quad w\,\bar{k} \tag{3.6}$$

$$\bar{\dot{q}} = \dot{q}_x\bar{i} + \dot{q}_y\bar{j} + \dot{q}_z\bar{k} \tag{3.7}$$

where the symbols, $\dot{q}_x$, $\dot{q}_y$ and $\dot{q}_z$, represents the components of the heat flux vector, $\bar{\dot{q}}$, and the symbols, u, v and w, the velocity components described earlier. The components of the heat flux vector, for Newtonian models, are defined by Fourier's law, which can be expressed mathematically in the form,

$$\begin{aligned} \dot{q}_x &= -k\frac{\partial T}{\partial x} \\ \dot{q}_y &= -k\frac{\partial T}{\partial y} \\ \dot{q}_z &= -k\frac{\partial T}{\partial z} \end{aligned} \tag{3.8}$$

in Equations (3.2 to 3.5) the shear stresses are best described through the use of the symmetric tensor quantity, $\hat{\tau}$, such that,

$$\hat{\tau} = \begin{bmatrix} \tau_{xx} & \tau_{xy} & \tau_{xz} \\ \tau_{yx} & \tau_{yy} & \tau_{yz} \\ \tau_{zx} & \tau_{zy} & \tau_{zz} \end{bmatrix} \tag{3.9}$$

in Equation (3. 9) the six independent components, $\tau_{xx}, \tau_{xy}, \tau_{yy}, \tau_{zx}, \tau_{zy}$ and τ_{zz}, are the local shear stresses for Newtonian fluids, and are defined as follows:

$$\tau_{xx} = \frac{2}{3}\mu(\nabla V) + 2\mu\frac{\partial u}{\partial x} \tag{3.10}$$

$$\tau_{yy} = \frac{2}{3}\mu(\nabla V) + 2\mu\frac{\partial v}{\partial y} \tag{3.11}$$

$$\tau_{zz} = \frac{2}{3}\mu(\nabla V) + 2\mu\frac{\partial w}{\partial z} \tag{3.12}$$

$$\tau_{xy} = \tau_{yx} = \mu\left(\frac{\partial u}{\partial y} + \frac{\partial v}{\partial x}\right) \tag{3.13}$$

$$\tau_{xz} = \tau_{zx} = \mu\left(\frac{\partial u}{\partial z} + \frac{\partial w}{\partial x}\right) \tag{3.14}$$

$$\tau_{yz} = \tau_{zy} = \mu\left(\frac{\partial w}{\partial y} + \frac{\partial v}{\partial z}\right) \tag{3.15}$$

In an effort to provide mathematical closure to the system of NS equations, appropriate expressions that represent the fluid model must also be provided. In this analysis and available in AVUS and FLUENT are the following fluid models,

$$P = \rho RT \tag{3.16}$$

$$e = C_v T + \frac{u^2 + v^2 + w^2}{2} \tag{3.17}$$

$$\mu = \mu_\infty \left(\frac{T}{T_\infty}\right)^{3/2} \frac{T_\infty + 100}{T + 100} \tag{3.18}$$

$$k = f(\mu) \tag{3.19}$$

symbols of interest to Equations (3.16 and 3.17) are e, C_v, μ and k. These symbols represent the internal energy, the specific heat at constant volume of the fluid, the viscosity and the thermal conductivity of the fluid. In this analysis, the viscosity of the

fluid is evaluated through the use of Sutherland's Law, equation (3.18), where μ_∞ and T_∞ are the freestream properties of viscosity and temperature of the incoming fluid.

Equations (3.1 to 3.18) form a closed system of partial differential equations, which must be solved in combinations with an appropriate set of initial and boundary conditions. The solution to these equations is by no means a simple task. Even when these equations are solved, they do not provide information on turbulence flows. In both FLUENT and AVUS, these equations are transformed into a system of algebraic equations and solved iteratively. A description of the solution process is described in the next section.

It is of interest to note that other equations representing turbulence models (Elamin, 2008), are usually coupled to the NS equations, to form an even more complex set of partial differential equations. The importance of these equations lies in their ability to provide very realist solutions to fluid dynamic problems, and especially those that involve turbulence. These equations are described in a proceeding section.

Solving the NS Equations (3.1 to 3.19) is not a simple task, as these equations must be solved under specified boundary and initial conditions. The major challenges in solving the NS-Equations lie in identifying a couple set of numerical configuration, flow domain, boundary conditions and grid representations that best describe the flowfield of interest. Statistical evidence to date has shown that in most cases, identifying the best combination of grids, numerical configuration and other NS requirements is rather an art and less of a science (Clarke, 2005). In this respect the GUI based, commercially available CFD tools have a great advantage over their research based alternatives. With

GUI based tools, users have the option to add equations and models, or make assumptions and reduce equations and models that apply to the NS Solver through multiple and integrated clicks of a mouse. In research based tools, even though these options are available, they are often not easier to implement. The model reduction or enhancement process is best described in Figure 3.1 (Alexandrov, 2010).

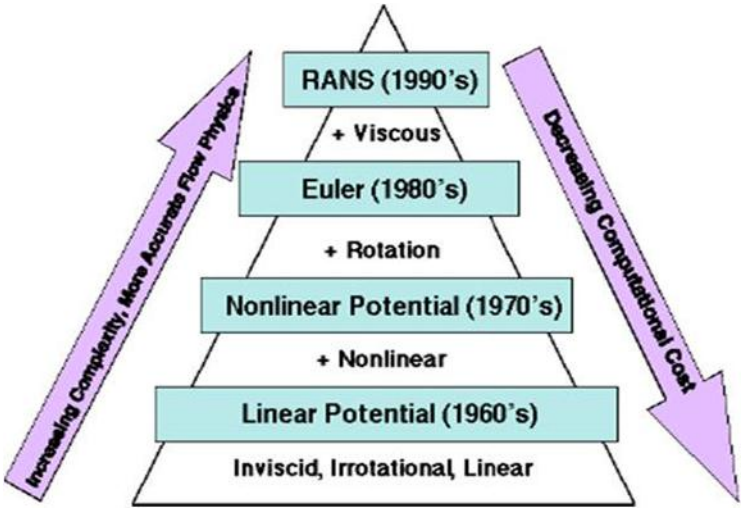

Figure 3.1. Fidelity Model Hierarchy

The final flowfield solution obtained from the NS-Solver is highly dependent on the use of the available tool. As illustrated in Figure 3.1, the addition of equations and models to the NS solver, representing turbulence, increases the complexity of the solver but enhances the accuracy of the solution. In contrast, the reduction of equations and fluid models, for example, reduction from a viscous to an inviscid model, usually reduces the

complexity of the NS solver. This increases the likely hood of a converged solution and delivers less physics-based accuracy from the problem of interest. A major objective of this study is the solution of the internal flowfield of a scramjet configuration designed at NCAT, as such great care was exercised in the choice of the available fluid dynamic models.

3.2.1 Turbulence Models. Turbulent flows are characterized by velocity fields which fluctuate rapidly both in space and time. Since these fluctuations occur over several orders of magnitude it is computationally very expensive to construct a grid which directly simulates both the small scale and high frequency fluctuations for problems of practical engineering significance. Two methods can be used to eliminate the need to resolve these small scales and high frequencies, namely, Reynolds Averaging and Filtering.

In the Reynolds Averaged approach all flow variables that are divided into a mean component and a rapidly fluctuating component. Then all equations are time averaged to remove the rapidly fluctuating components. For the continuity equation the new equation is identical to the original equation, except that the transported variables now represent the mean flow quantities. In the momentum equation however new terms appear which involve the mean values of products of rapidly varying quantities. These new terms are known as the Reynolds Stresses. Solution of the Reynolds Averaged Navier-Stokes (RANS) equation initially involves the construction of suitable models to represent these Reynolds Stresses. One approach to this problem is to treat the time averaged terms as additional viscous stresses produced by the turbulence in the flow. In the Boussinesq

approach, the Reynolds Stresses are assumed to have a form identical to the viscous stresses in the momentum equation, apart from a multiplicative term known as the turbulent viscosity, μ_T. Note that this approach assumes that the Reynolds Stresses are isotropic, which is known to be untrue in many cases. The problem then reduces to finding an expression for μ_T. The two models of interest to this study are the Spalart-Allmaras and the Reynolds Stress models. These models are described in the next two subsections.

3.2.2 The Spalart-Allmaras Model. FLUENT provides several turbulence models based on the Boussinesq approach: the Spalart-Allmaras model, the k-ε model, and the k-ω model. The Spalart-Allmaras model is of interest to this analysis. The Spalart-Allmaras model is a relatively simple one-equation model that solves the transport equation for the kinematic eddy (or turbulent) viscosity. This model embodies a relatively new class of one-equation models in which it is not necessary to calculate a length scale related to the local shear layer thickness. The Spalart-Allmaras model was designed specifically for aerospace applications involving wall-bounded flows and has been shown to give good results for boundary layers subjected to adverse pressure gradients (Balakrishnan, 1990).

The transported variable in the Spalart-Allmaras model,$\tilde{\upsilon}$, is identical to the turbulent kinematic viscosity except in the near-wall (viscous-affected) region. The transport equation for $\tilde{\upsilon}$ is defined as follows:

$$\frac{\partial}{\partial t}\left(\rho\tilde{\nu}\right)+\frac{\partial}{\partial x_i}\left(\rho\tilde{\nu}u_i\right)=G_\nu+\frac{1}{\sigma_{\tilde{\nu}}}\left[\frac{\partial}{\partial x_j}\left\{\left(\mu+\rho\tilde{\nu}\right)\frac{\partial\tilde{\nu}}{\partial x_j}\right\}+C_{b2}\rho\left(\frac{\partial\tilde{\nu}}{\partial x_j}\right)\right]-Y_\nu+S_{\tilde{\nu}} \quad (3.20)$$

where G_v is the production of turbulent viscosity and Y_v is the destruction of turbulent viscosity that occurs in the near-wall region due to wall blocking and viscous damping. $\sigma_{\tilde{\upsilon}}$ and C_{b2} are constants and υ is the molecular kinematic viscosity. $S_{\tilde{\upsilon}}$ is a user-defined source term.

Besides the Spalart-Allmaras model, there are two other algebraic models; the *k*-ε model and the *k*-ω models. Both models are inherently more complicated, as they involve finding solutions to two additional model transport equations, one for the turbulent kinetic energy *k*, and one for the rate of dissipation of the turbulent kinetic energy ε. In the case of the *k*-ω model, an equation for ω (where ω is defined by ω = ε / *k*). The turbulent viscosity μ_T is then calculated from an expression involving *k* and ε for the *k*-ε model, or *k* and ω for the *k*-ω model.

3.2.3 The Reynolds Stress Model. A turbulence model which avoids making the isotropic Boussinesq approximation is the Reynolds Stress Model (RSM). This is the most elaborate turbulence model that FLUENT provides. The RSM also finds a solution to the Reynolds-Averaged Navier-Stokes equation by solving additional transport equations for each of the individual Reynolds stresses, as well as an equation for the dissipation rate. This means that four additional transport equations are required in 2D flows and seven additional transport equations must be solved in 3D flows. Since the RSM accounts for the effects of streamline curvature, swirl, rotation, and rapid changes in strain rate in a more rigorous manner than the one-equation (Spalart-Allmaras) and the two-equation (*k*- ε and *k*- ω) models it has greater potential to give accurate predictions for complex flows. The accuracy of the RSM predictions are still limited, however, by

the closure assumptions used to model various terms in the exact transport equations for the Reynolds stresses. For this reason the RSM does not always provide results which are superior to those of simpler models for all flows. The equations that best describe the RSM model are as follows:

$$\frac{\partial}{\partial t}\left(\rho\overline{u_i^{'}u_j^{'}}\right)+C_{ij}=D_{T,ij}-P_{ij}-G_{ij}+\phi_{ij}-\varepsilon_{ij}-F_{ij}+S_{user} \tag{3.21}$$

Where the first term in Equation (3.21) represents the local time derivative. Furthermore, C_{ij}, $D_{L,ij}$, P_{ij}, F_{ij}, $D_{T,ij}$, G_{ij}, ϕ_{ij},, ε_{ij}, *and* S_{user} represents the Convection, Molecular Diffusion, Stress Production, Production of System Rotation, Turbulent Diffusion, Buoyancy Production, Pressure Strain, Dissipation, and the User-Defined Source terms respectfully. The exact transport equation for the transport of the Reynolds stresses, $\rho\overline{u_i'u_j'}$, as seen in Equation (3.21), may be expanded as shown in Equation (3.22):

$$\begin{aligned}\frac{\partial}{\partial t}\left(\rho\overline{u_i^{'}u_j^{'}}\right)+\frac{\partial}{\partial x_k}\left(\rho u_k\overline{u_i^{'}u_j^{'}}\right)&=-\frac{\partial}{\partial x_k}\left[\rho\overline{u_i^{'}u_j^{'}u_k^{'}}+\overline{p\left(\delta_{kj}u_i^{'}+\delta_{ik}u_j^{'}\right)}\right]\\&+\frac{\partial}{\partial x_k}\left[\mu\frac{\partial}{\partial x_k}\left(\overline{u_i^{'}u_j^{'}}\right)\right]-\rho\left(\overline{u_i^{'}u_j^{'}}\frac{\partial u_j}{\partial x_k}+\overline{u_j^{'}u_k^{'}}\frac{\partial u_i}{\partial x_k}\right)-\rho\beta\left(g_i\overline{u_i^{'}\theta}+g_j\overline{u_i^{'}\theta}\right)\\&+\overline{p\left(\frac{\partial u_i^{'}}{\partial x_j}+\frac{\partial u_j^{'}}{\partial x_i}\right)}-2\mu\frac{\partial u_j^{'}}{\partial x_i}\frac{\partial u_i^{'}}{\partial x_j}-2\rho\Omega_k\left(\overline{u_j^{'}u_m^{'}\varepsilon_{ikm}}+\overline{u_i^{'}u_m^{'}\varepsilon_{jkm}}\right)+S_{user}\end{aligned} \tag{3.22}$$

Within the many terms in the exact equation, C_{ij}, $D_{L,ij}$, P_{ij}, *and* F_{ij} do not require any modeling. However, $D_{T,ij}$, G_{ij}, ϕ_{ij}, *and* ε_{ij} need to be modeled to close the equations. The following equations describe the modeling assumptions required to close the equation set. FLUENT simplifies the generalized gradient-diffusion model of Daly and Harlow (FLUENT,2010).

$$D_{T,ij} = \frac{\partial}{\partial x_k}\left(\frac{\mu_t}{\sigma_k}\frac{\partial \overline{u_i' u_j'}}{\partial x_k}\right) \tag{3.23}$$

where the turbulent viscosity, μ_t, is described using Equation (3.23) and σ_k holds the value of 0.82. In order to model the pressure strain term effectively, the quadratic pressure-starin model can be selected as an option in FLUENT. This model is best written as follows:

$$\phi_{ij} = -\left(C_1\rho\varepsilon + C_1^* P\right)b_{ij} + C_2\rho\varepsilon\left(b_{ij}b_{kj} - \frac{1}{3}b_{mn}b_{mn}\delta_{ij}\right) + \left(C_3 - C_3^*\sqrt{b_{ij}b_{ij}}\right)\rho k\delta_{ij}$$

$$+ C_4\rho k\left(b_{ik}S_{jk} + b_{jk}S_{ik} - \frac{2}{3}b_{mn}S_{mn}\delta_{ij}\right) + C_5\rho k\left(b_{ik}\Omega_{jk} + b_{jk}\Omega_{ik}\right) \tag{3.24}$$

where b_{ij} is the Reynolds-stress anisotropy tensor defined as

$$b_{ij} = -\left(\frac{-\rho\overline{u_i' u_j'} + \frac{2}{3}\rho k\delta_{ij}}{2\rho k}\right) \tag{3.25}$$

The mean strain rate, S_{ij}, is defined as

$$S_{ij} = \frac{1}{2}\left(\frac{\partial u_j}{\partial x_i} + \frac{\partial u_i}{\partial x_j}\right) \tag{3.26}$$

The mean rate-of-rotation tensor, Ω_{ij} , is defined by

$$\Omega_{ij} = \frac{1}{2}\left(\frac{\partial u_i}{\partial x_j} + \frac{\partial u_j}{\partial x_i}\right) \tag{3.27}$$

Where the constants are $C_1 = 3.4, C_1^* = 1.8, C_2 = 4.2, C_3 = 0.8, C_3^* = 1.3, C_4 = 1.25, C_5 = 0.4$. The production terms due to buoyancy are modeled as:

$$G_{ij} = \beta \frac{\mu_t}{\mathrm{Pr}_t} \left(g_i \frac{\partial T}{\partial x_j} + g_j \frac{\partial T}{\partial x_i} \right) \tag{3.28}$$

where Pr_t is the turbulent Prandtl number for energy, with a default value of 0.85. In general, when the turbulence kinetic energy is needed for modeling a specific term, it is obtained by taking the trace of the Reynolds stress tensor:

$$k = \frac{1}{2} \overline{u_i' u_j'} \tag{3.29}$$

The dissipation tensor, ε_{ij}, is modeled as

$$\varepsilon_{ij} = \frac{2}{3} \delta_{ij} \left(\rho \varepsilon + Y_M \right) \tag{3.30}$$

where $Y_M = 2\rho\varepsilon M_t^2$ is an additional "dilatation dissipation" term according to the model by Sarkar (Balakrishnan, 1990). The turbulent Mach number in this term is defined as

$$M_t = \sqrt{\frac{k}{a^2}} \tag{3.31}$$

where $a \equiv \sqrt{\gamma RT}$ is the speed of sound. This compressibility modification always takes effect when the compressible form of the ideal gas law is used. The turbulent viscosity, μ_t, is computed as:

$$\mu_t = \rho C_\mu \frac{k^2}{\varepsilon} \tag{3.32}$$

where C_μ = 0.09.

3.2.4 Filtering Reynolds Stress Models. It is, of course, necessary to use the RSM when the flow features of interest are the result of anisotropy in the Reynolds stresses. However, an alternative approach to Reynolds averaging is filtering. The idea

behind this approach is to filter the time-dependent Navier-Stokes equation in either Fourier (wave-number) space or configuration (physical) space. This filtering process effectively filters out turbulent eddies whose scales are smaller than the filter width, which is usually taken to be the mesh size. As with Reynolds averaging however, the filtering process creates additional unknown terms which must be modeled in order to provide closure to the set of equations. This approach is known as Large Eddy Simulation (LES) because the fluctuations of the large scale eddies (those having a size comparable to the main geometry of the flow) are numerically resolved, rather than being averaged out as in the RANS approach. The attraction of LES is that, by modeling less of the turbulence (and solving more), the error introduced by the turbulence model will be reduced.

FLUENT provides two methods to model the subgrid-scale stresses resulting from the filtering operation: the Smagorinsky-Lilly model and the RNG (ReNormalization Group) subgrid-scale model. All LES simulations require a lengthy time-dependent run so that statistics of the mean flow quantities can be gathered. LES simulations also require a relatively fine grid, and so the computational cost of LES simulations can be quite excessive.

3.3 The GAMBIT-FLUENT CFD Package

FLUENT 6.2 is a CFD software package that simulates fluid flow problems with varying degrees of fidelity. It uses the finite-volume method and therefore the integral form of the NS equations to solve the governing fluid dynamic equations. It also provides

the capability to use a variety of physically based fluid models; such as incompressible or compressible, inviscid or viscous and laminar or turbulent models. In addition, all geometric information and grid generation activities are done using the PPP tool, GAMBIT. In the most recent version of FLUENT, GAMBIT is bundled with FLUENT, into a single CFD tool.

3.3.1 GAMBIT Grid Deneration Software. The use of FLUENT 6.2 starts with the GAMBIT routine, and through the use of its GUI interface which is illustrated in Figure 3.2 (Riff, 2004). As noted in Figure 3.2, GAMBIT facilitates the construction of the geometric configuration of interest and the assignment of the appropriate boundary conditions through the use of menus and mouse clicks.

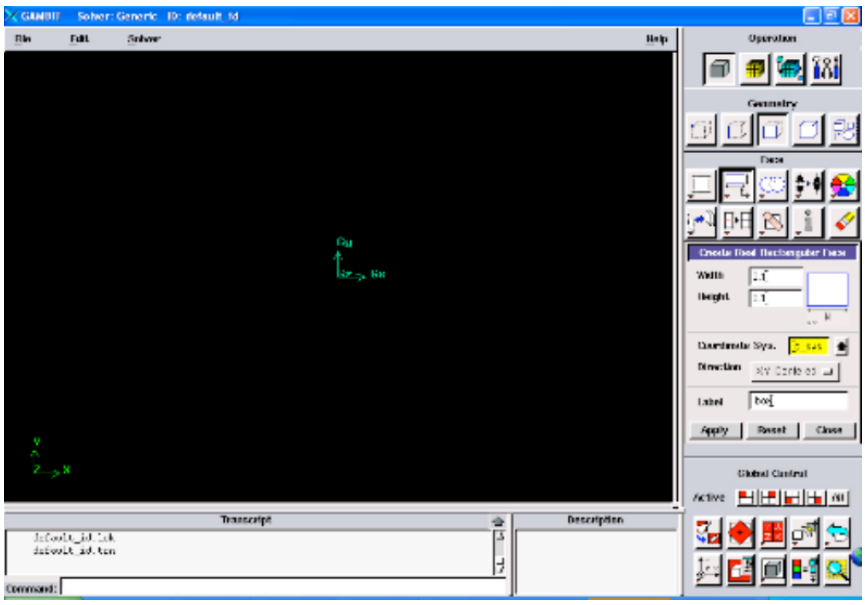

Figure 3.2. GAMBIT-Graphic User Interface

Further, GAMBIT allows for the definition and construction of both 2D and 3D flowfield domains. Illustrated in Figure 3.3 (Akbarzada, 2007) is a typical 3D flowfield domain generated through the use of GAMBIT. In addition, GAMBIT allows for the generation of the grids. GAMBIT is capable of creating two-dimensional (2D) surface mesh using triangular or quadrilateral elements, and three-dimensional (3D) volume mesh using a combination of hexahedral, tetrahedral, or prism elements.

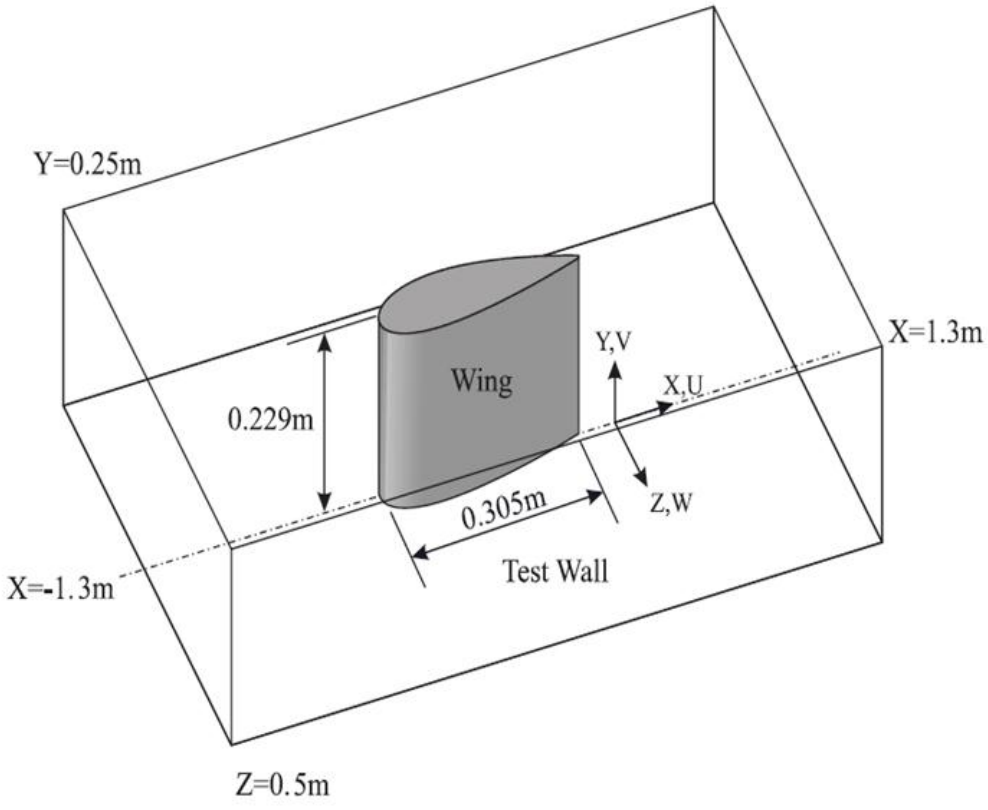

Figure 3.3. Typical 3D flowfield domain generated by GAMBIT

3.3.2 FLUENT Navier-Stokes Solver. Once the fluid domain has been meshed, the boundary and initial conditions are next selected and the appropriate fluid models, such as laminar or turbulent flows, are chosen. It is of interest to note that all selections and definitions are made through the use of the GUI. Finally, all appropriate data is then passed on to the NS solver in FLUENT. As described earlier, the governing equations (in integral form) for the conservation of mass, momentum, energy and all other relevant physical fluid models are applied to each discrete control volume and used to construct a set of non-linear algebraic equations for the discrete dependent variables. FLUENT then solves the complete set of coupled equations for all the control volumes on the mesh using either a segregated solver or a coupled solver (Clarke, 2005). In this approach the governing equations are solved sequentially. However, since these equations are non-linear they first have to be linearized. This can be done either implicitly or explicitly, although when using the segregated solution method within Fluent, the NS solver automatically linearises each discrete governing equation implicitly with respect to that equation's dependent variable. This produces a scalar system of equations containing only one equation per computational cell (Clarke, 2005). A point implicit (Gauss-Siedel) linear equation solver is then used in conjunction with an algebraic multigrid (AMG) method to solve the resultant scalar system of equations for the dependent variable in each cell. Since the equations are non-linear several iterations of the solution loop must be performed before a converged solution is obtained.

The segregated solver thus solves for a given fluid variable (for example U – the x component of velocity) by considering all cells at a single time. It then solves for the next

fluid variable (for example V – the y component of velocity) by again considering all cells at the same time. Each iteration of the solution loop consists of the following steps:

1) The values of the fluid variables at the cell centers are updated based on the current solution values.
2) The U, V and W velocity components of the momentum equation are each solved in turn using the current values for the pressure and the mass fluxes through each of the cell faces.
3) The pressure correction equation (a form of the continuity equation) is then solved to obtain the necessary corrections to the pressure and velocity fields so that the continuity equation is satisfied. This process is described in the next section.
4) Where appropriate, additional scalar equations (such as those describing transport of turbulence quantities) are solved.
5) A check for convergence.
6) The above steps are repeated until the convergence criteria are met (all residuals less than 10^{-6})

As described earlier, an equation for each component of the momentum equation and the continuity equation are solved sequentially. Once the three components of velocity have been calculated for each cell using this sequential system the velocities may not satisfy the continuity equation. So, a "Poisson-type" equation for a pressure correction is derived from the continuity equation and the linearized momentum equations (Clarke, 2005). This pressure correction equation is then solved to obtain the necessary corrections to the pressure and velocity fields such that continuity is satisfied.

Although the pressure variable appears in each of the component momentum equations each of these equations is solved by treating the relevant component of velocity as the unknown variable, and the pressure field in the equation is taken to be that from the previous iteration. In this sequential procedure, the continuity equation is used as an equation for the pressure. However, pressure does not appear explicitly in the continuity equation for incompressible flows (which are the only flows considered in this report). Instead, a procedure must be devised to introduce pressure into this equation. FLUENT provides methods based on the SIMPLE (Semi-Implicit Method for Pressure-Linked Equations) family of algorithms to do this, refer to Patankar for details.

The basic SIMPLE algorithm uses a relationship between velocity and pressure corrections to enforce mass conservation and to obtain the pressure field. The SIMPLEC algorithm (SIMPLEConsistent) is a variation of the SIMPLE algorithm which uses a more refined expression for the variable flux through each of the cell faces. This can accelerate convergence in some problems where the pressure-velocity coupling is the main deterrent to obtaining a solution (Patankar, 1972). The PISO pressure-velocity coupling scheme (Pressure-Implicit with Splitting of Operators) is also part of the SIMPLE family of algorithms and is based on a higher degree of approximation for the relation between the corrections for pressure and velocity (Issa, 1986). The PISO algorithm takes a little more CPU time per solver iteration but it can dramatically decrease the overall number of iterations required for convergence, especially for transient problems. The PISO algorithm also allows FLUENT to obtain solutions on

highly skewed meshes in approximately the same number of iterations as required for more orthogonal meshes.

3.3.3 FLUENT Computational Grid requirements. The degree of resolution required of the computational grid depends somewhat on the choice of turbulence model to be used in the simulation. The *k*-ε models, RSM, and LES models are primarily valid for turbulent core flows. For flow in the regions somewhat far from walls, the Spalart-Allmaras and *k*-ω models were designed to be applied throughout the boundary layer, provided that the near-wall mesh resolution is sufficient. The *k*-ε models can still be applied to wall bounded flows, however, by using the concept of wall functions. In this approach use is made of the universal behavior of equilibrium boundary layer flows. It is well known that the near-wall region in an equilibrium boundary layer can be divided into several distinct regions (Pope, 2000). Very close to the wall, the flow is almost laminar and the molecular viscosity plays a dominant role in momentum transfer. This region is known as the "viscous sublayer". At much greater distances from the wall, but still well within the boundary layer, molecular viscosity plays no part and the velocity profile is determined purely by the turbulent viscosity.

This is known as the outer layer, or fully-turbulent layer. In between the viscous sublayer and the fully turbulent layer there is an interim layer where the effects of molecular viscosity and turbulence are equally important. This is known as the buffer layer or blending region. When standard wall functions are used the viscosity affected inner region (viscous sublayer and buffer layer) is not resolved. Instead, semi-empirical formulas are used to bridge the viscosity affected region between the wall and the fully

turbulent region. The use of wall functions thus obviates the need to modify the turbulence model to account for the presence of the wall. In practice, this means that the center of the cell closest to the wall must lie above a certain height. If $y+$ denotes the (scaled) co-ordinate direction normal to a solid wall and P denotes the center point of the cell closest to the wall, then $y+P$ should lie in the range $30< y+P<100$. If this criterion is satisfied then the boundary conditions can be satisfied at the point P by using the universal "log-law" for the mean velocity. Appropriate values for the other variables can also be derived at this location from the universal nature of the flow in this region.

3.3.4 Technical Survey of FLUENT Capability. In an effort to illustrate the use of the combined GAMIBIT-FLUENT package as a CFD tool with the capability to analyze the problem of interest to this thesis, this discussion will continue as it relates to the solution of a 2D supersonic inlet configuration (Clarke, 2005), and one that has many of the physical features of the problem of interest to this thesis (Clarke and Akbarzada). The simplest form of staged compression is the two-shock inlet in which a single angle wedge or cone projects forward of the duct. The 2D supersonic inlet problem that is used in this illustration was described in great details in Reference (Issa, 1986). For an explanation and illustration of the boundary conditions refer to FLUENT. Apart from the quantities of boundary conditions of inlet 1 which will be given in next parts, the boundary conditions at the inlet is set to 40 kPa static pressure value and mach number = 2.5.

The flow is also assumed to be arriving to the computational domain as normal. At the exit plan, static pressure boundary is used. In this study the flow of the interior part is

directed to a subsonic combustion chamber. The effect of combustion is simulated by imposing constant pressure levels associated with combustion of the exit of the engine inlet. All flow parameters are extrapolated to the top of the computational domain and it is taken far enough from the engine inlet, so the oblique shocks generated from the spike leading edge and cowl lip cannot reach this boundary. At the center line (from inlet plan to the leading edge of the spike), a symmetry condition is enforced. Using GAMBIT, the 2D subsonic inlet is constructed as illustrated in Figure 3.4 (Akbarzada, 2007), the flowfield domain is identified and then divided into computational grid points.

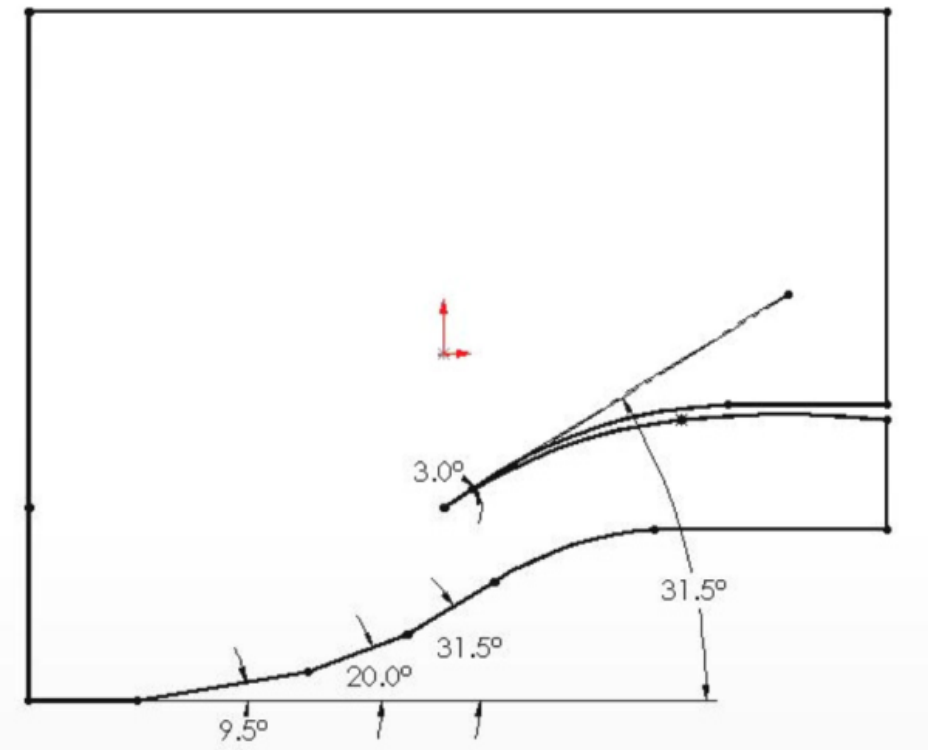

Figure 3.4. 2D Supersonic Inlet

These grid points in turn form a large number of discrete control volumes (also known as cells) on the computational mesh. The NS equations are then solved with respects to the primitive variables on the computational mesh. The computational mesh of interest to this example is illustrated in Figure 3.5 (Akbarzada, 2007).

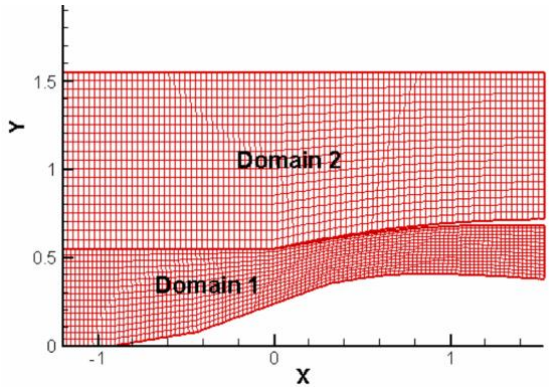

Figure 3.5. 2D Inlet Computational Grid

This problem has been constructed through the use of GAMBIT and solved by FLUENT (Akbarzada, 2007). The results are in very good agreements with the literature (Akbarzada, 2007) and the critical condition is obtained at the same back pressure that is presented by the literature (Akbarzada and Pope). The contours of mach number and static pressure for inlet 2 are shown in Figures 3.6 and 3.7, (Akbarzada , 2007) respectively. The flow enters to the engine at a mach number of about 0.5, which is usually recommended for subsonic combustion jet engines, (Goldsmith, 1999).

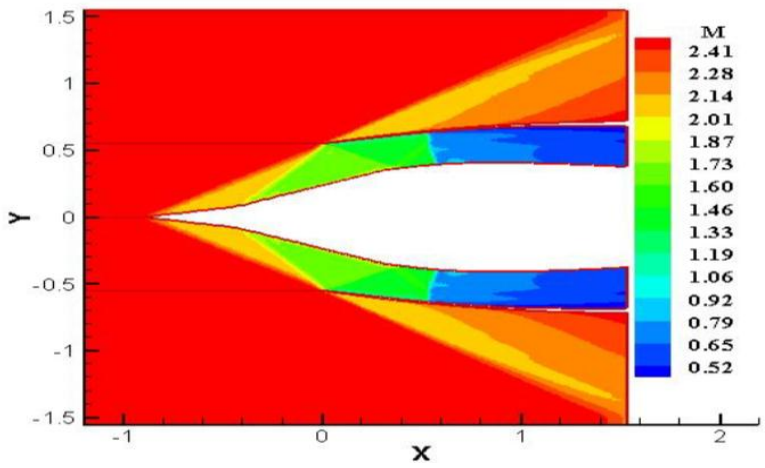

Figure 3.6. Mach Number Contours

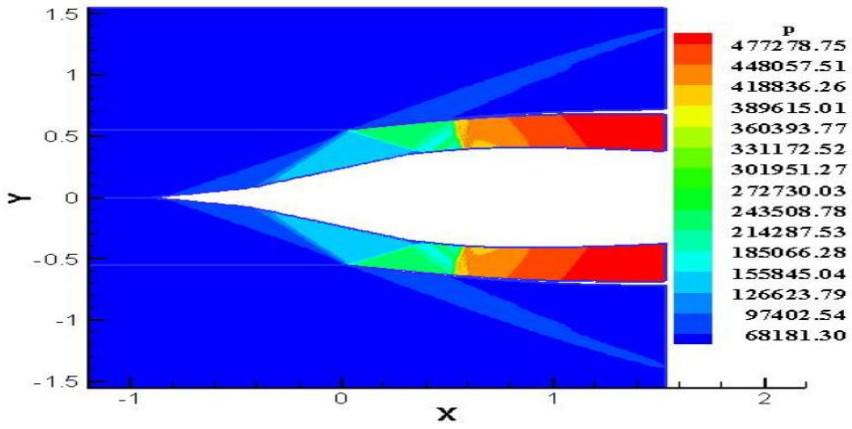

Figure 3.7. Static Pressure Contours

The FLUENT results described herein, are supported by numerous examples of the use of FLUENT as a reliable and user friendly CFD tool. These efforts also serve to justify the use of FLUENT in this analysis.

3.4 Gridgen-AVUS CFD Package

The Gridgen-AVUS CFD Tool combination was also used to analyze the problem of interest to this thesis. However, since Gridgen functions in much the same manner of GAMBIT, no further description of this software will be given. On the other hand, AVUS is a Research based CFD Tool with the capability to deliver very high quality results, as such a brief description of this code is warranted.

3.4.1 AVUS Navier-Stokes Solver. Since AVUS is a NS Solver, it functions in much the same manner as FLUENT. However, the fundamental algorithm of AVUS is the finite-volume, cell-centered, first-order accurate in space and time, grid-aligned exact Riemann solver of Godunov (Gottlieb, 1988). Godunov's exact Riemann solver is very expensive, so the exact Riemann solution method of Gottlieb and Groth (van Leer, 1979) is used in AVUS. Second-order accuracy in space is patterned after van Leer's (Tomaro, 1997) MUSCL scheme where the flow state is assumed to vary linearly within each cell. The linear variations (gradients) are constructed by a least squares method that, in turn, is solved by QR factorization. First- and second-order temporal accuracy is achieved via the unconditionally stable point-implicit scheme as implemented by Tomaro and others. (MacCormack, 1969). Second-order accurate viscous terms patterned after the work of MacCormack (Spalart, 1992) are added to the above inviscid algorithm to yield a Navier-Stokes solver. The temporal accuracy of the viscous terms is equivalent to that of the inviscid terms. The one-equation turbulence models of Spalart-Allmaras (Wilcox, 1998) and the Detached Eddy Simulation (DES) model of Spalart (Wilcox and Consantinescu) along with the (Wilcox, 1998) k-omega two-equation turbulence model (Ansari, 1996)

Menter's baseline two-equation turbulence model (Menter, 1993) and Menter's baseline model with the SST correction (Menter, 1993) are available to model the fine scale effects of turbulence. Wall functions are available for adiabatic no-slip wall boundary conditions for all the turbulence models. In the creation of AVUS, much effort was devoted to boundary conditions to achieve high accuracy with robustness and flexibility. Interested readers may also refer to the papers of Ansari and Strang (Ansari, 1996) and Grismer and others (Karypis, 1995) for additional discussion of the underline numerical theories within AVUS.

In practice, AVUS can treat two-dimensional, axi-symmetric and three-dimensional problems. The grid can be composed of cells of arbitrary types, i.e., tetrahedrals, quadrilaterals, pyramids, or triangles. Different cell types are permitted within the same grid. The set of boundaries forming each cell, called faces, can also be arbitrary (triangles, pentagons, lines, etc.), though each cell boundary face should be convex. Further, the grids may be decomposed into sub-domains, called groups or zones, permitting parallel processing where each zone resides on a separate processor. The information described in this sub-section is more commonly found in The AVUS User's Manual.

3.4.2 AVUS Grid File. An AVUS grid file specifies the geometry of the problem of interest as well as the connectivity information and boundary condition placement. *AVUS* requires certain grid information to be organized in a specific manner. So long as the grid meets these prescribed criteria, it can be created by any method. At Wright-Patterson Air Force Base/Air Force Research Laboratory (WPAFB/AFRL), the

interactive grid generators are, Gridgen, TOPDUUG, TETMESH, VGRID, and TRI2D. TETMESH (Kennon, 1992), was developed by COMCO under contract with AFRL/VAAC, and VGRID (Parikh, 1992), developed by Vigyan under contract with the NASA Langley Research Center, are used to create three-dimensional unstructured grids. With the exception of the VGRID meshes, AVUS reads the resulting grids directly. Recently, AFRL introduced the '*Blacksmith,'* a GUI utility code which is capable of converting grid files generated form an arbitrary grid generation code into a format compatible to AVUS.

3.4.3 AVUS standard Input Data. To assist users in creating a job file for submission to AVUS, a GUI called *Ligase* was recently developed. It is of interest to note that the Standard Input Data file is not the same as the grid file. Ligase was written using X-motif and the C programming language. The main window of the Ligase utility code is shown in Figure 3.8 (AFRL, 2007). New job files can be created or existing job files modified. Utilities included are: unit systems conversion of single values or the entire job file, and a calculator to determine pressure or temperature from Reynolds number and other quantities. *Ligase* also allows the creation and modification of Boundary Condition files. In comparison to GAMBIT^{TM}, Ligase is still a primitive tool.

The AVUS input data deck, or standard input, forms the majority of the so-called job file. The standard input is divided into seven blocks, each with entries controlling similar functions within AVUS. In the following description of the standard input, each block heading is in boldface; and each entry heading is italicized. Terms within the square brackets, [], denote the range of valid input. Default values, when they exist, are

displayed within the triangular brackets, <>, and are invoked with a negative entry. Entries with a decimal point are considered floating point variables; and those without are considered integer variables.

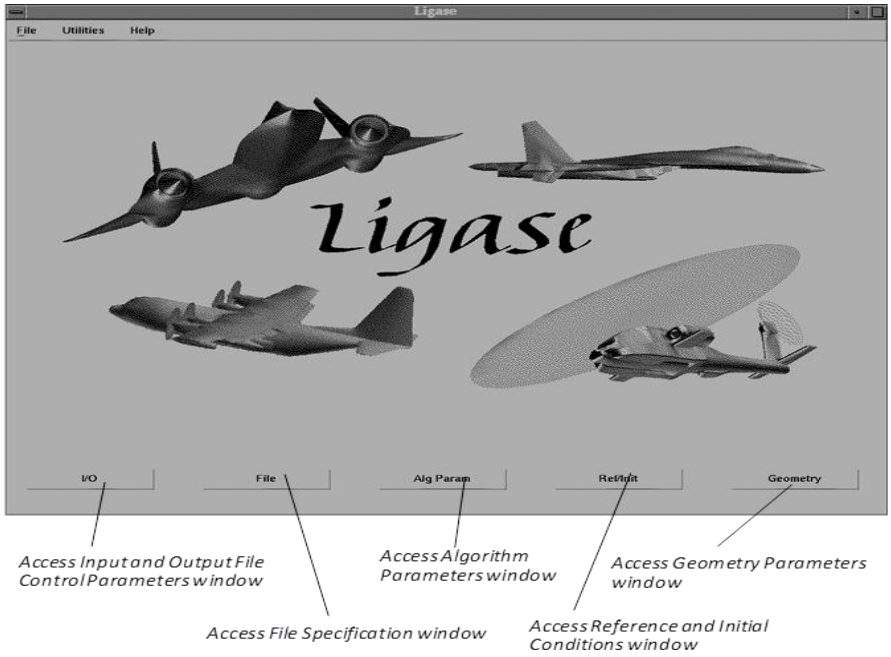

Figure 3.8. The main window of the AVUS-Ligase utility code

3.4.4 Technical survey of AVUS Capabilities. A CFD investigation was conducted on a variable geometry supersonic mixed compression inlet (Atkinson, 2007). Please refer to Figure 3.9 (Atkinson, 2007). The regulating features of the inlet are a variable compression ramp, diffuser, and throat. The compression ramp is designed to rotate about the y-axis from 0-12 degrees. The throat is also designed for varying heights,

ranging from 0.75 to 1.5 inches. As illustrated in Figure 3.9, the inlet is coupled with the trailing edge of the variable geometry diffuser. Experience has showed that during operations, this inlet produced relatively strong shock-waves and turbulent boundary layer interactions that cause the boundary layer to separate and diminish the overall performance of the inlet.

In an effort to improve the performance of this inlet and to counter the adverse effects of shockwave turbulent boundary layer interactions, the inlet was modified. The modified inlet is equipped with several conventional bleed systems located along: the compression ramp, along the interior of the throat, and along the upper, lower, and sidewall surfaces. As an alternative to boundary layer bleed, the baseline inlet model was fitted with micro-ramps as a potentially more efficient method of turbulent boundary layer separation control (Atkinson, 2007).

In an effort to evaluate the performance of this modified inlet, a CFD evaluation was conducted. All numerical simulations were conducted using the AFRL developed AVUS CFD Solver. During all CFD computations, the compressible 3D steady state Navier-Stokes equations coupled with the (Wilcox, 1998) k-ω two equation turbulence model were solved. The bleed surfaces and micro-ramps are designed to be removable, so that numerical baseline testing can be easily incorporated. A major objective of this CFD analysis was to examine several inlet performance characteristics, such as, total pressure recovery, mass flow, static pressures on the inlet surfaces, and flow distortion.

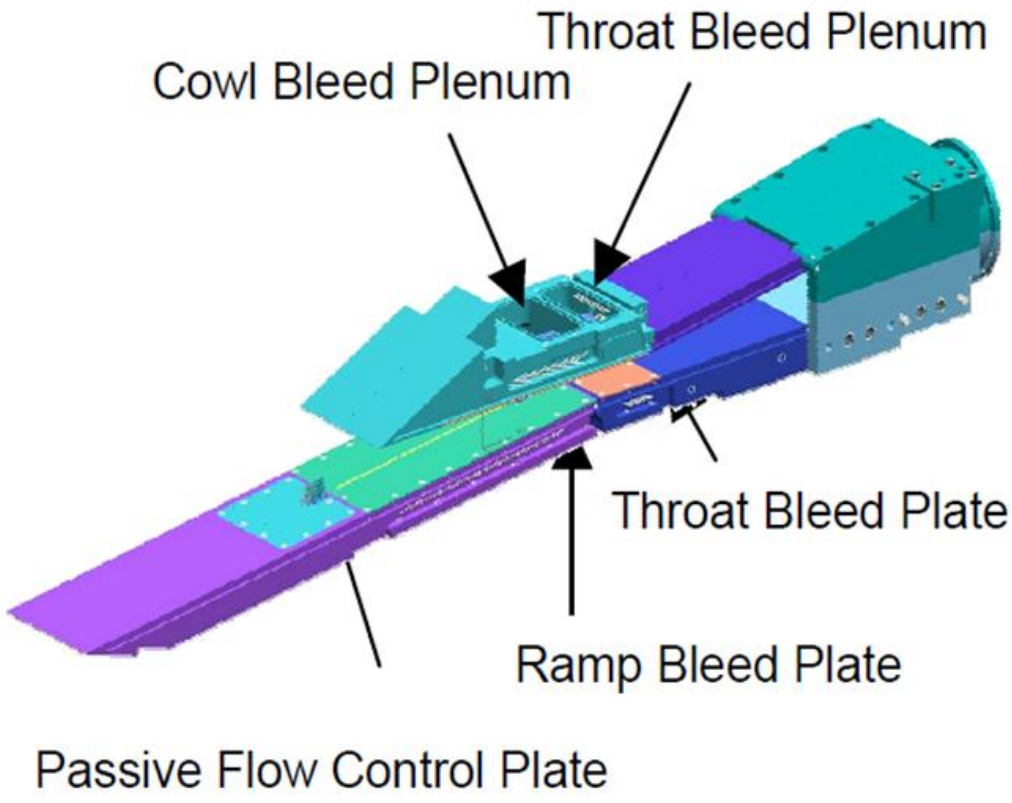

Figure 3.9. The Virtual SBLI CFD Configuration

As part of the inlet analysis (Atkinson, 2007), unstructured hybrid viscous computational grids were generated using ICEM-CFD, a commercial grid generation and PPP tool. The resulting grid consisted of prisms, pyramids, and tetrahedron elements. All CFD computations were conducted at a freestream mach number of 3.0 and Reynolds number of 2.71 million. The computational grid used in this study as illustrated in Figure 3.10 (Atkinson, 2007).

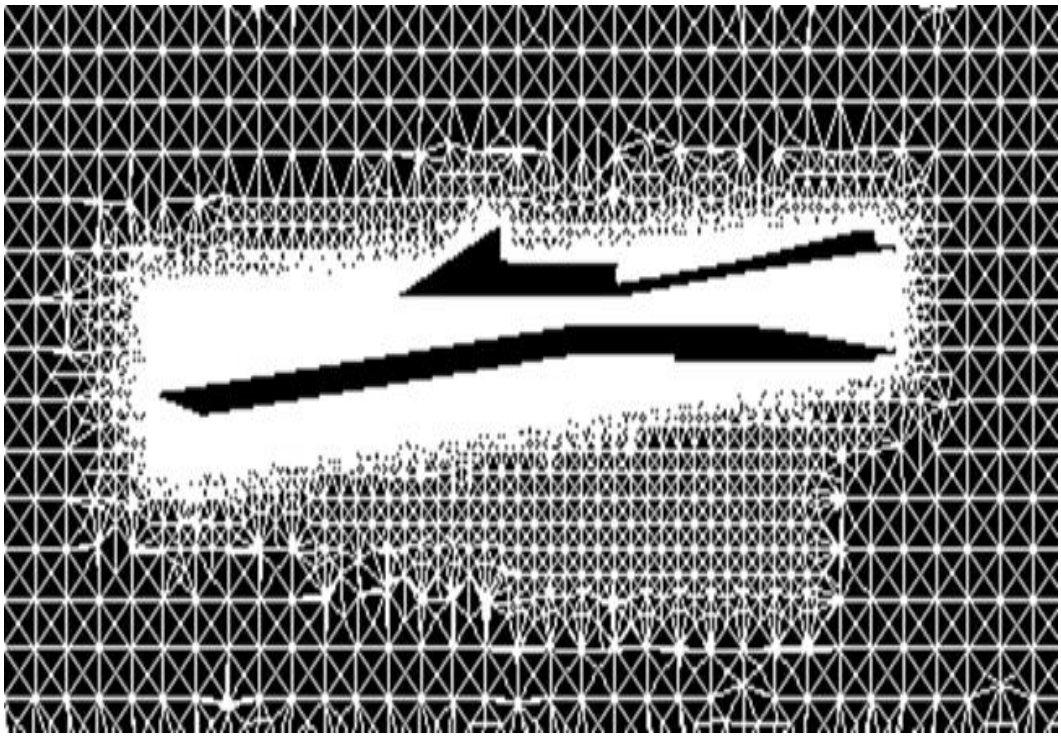

Figure 3.10. ICEM Grid

Additionally, sample results of this study are illustrated in Figures 3.11(Atkinson, 2007) and 3.12 (Atkinson, 2007), under the conditions of with and without bleeding. The results in Figures 3.11 and 3.12 are illustrated in the form of mach number contour plots. In the two cases illustrated in Figures 3.11 and 3.12 the ramp geometry remained consistent. The results of this study demonstrated that by controlling the shockwave turbulent boundary layer interactions in the inlet with micro-ramps can led to an over increase in the efficiency of the inlet (Atkinson, 2007). In addition, this example demonstrated that AVUS has the capability to evaluate the problem of interest to this thesis.

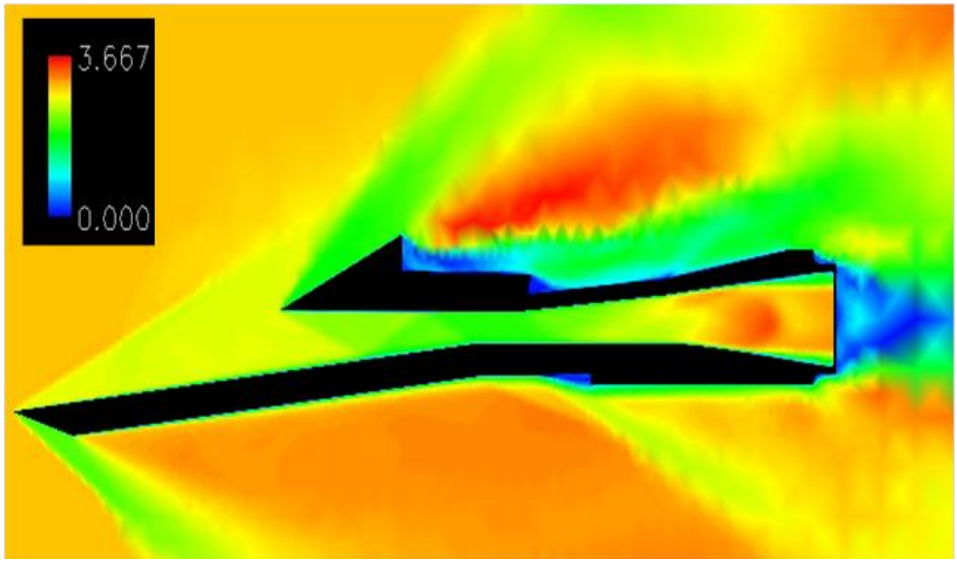

Figure 3.11. Contours of Mach Number, 6° Ramp without Bleed

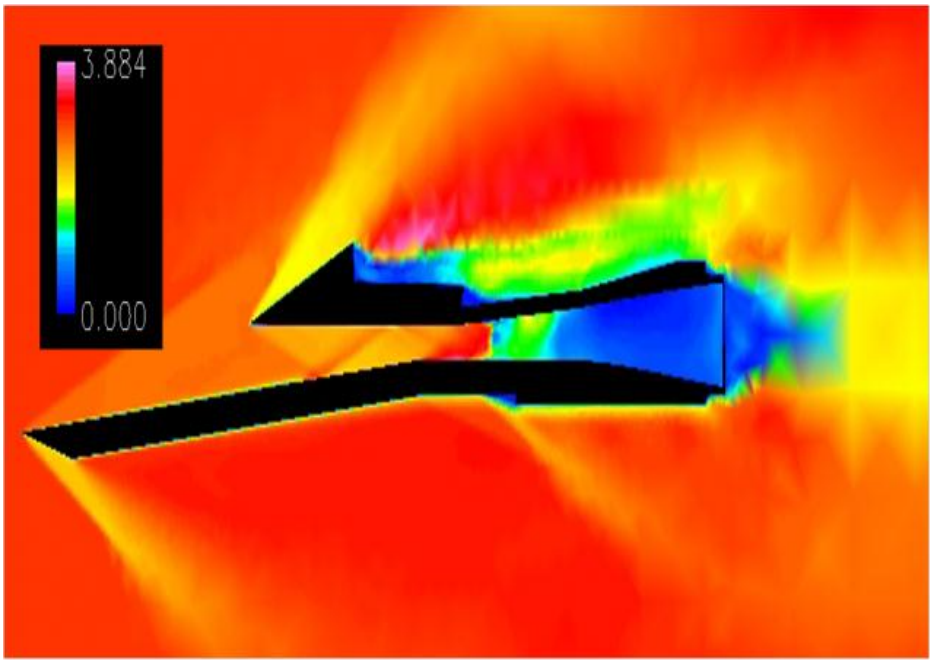

Figure 3.12. Contours of Mach Number with 6° Ramp and 2% Bleed

CHAPTER 4

COMPUTATIONAL FLUID DYNAMIC EVALUATIONS

At this point, it is important to recall that the major objective of this thesis is the independent validation of the hypersonic flowfield associated with an inlet that was inversely generated (Dhanasar, 2009). This inlet is illustrated in its entirety in Figure 4.1. It is also of interest to note that this inlet was previously evaluated at WPAB using a combination of the Gridgen-AVUS CFD tools (Ferguson, 2009). The results of the previous study indicated that the detailed resolution of the entire flowfield, which includes the internal flows of four identical tubes and the external flow associated with the inlet, require an enormous computational resources.

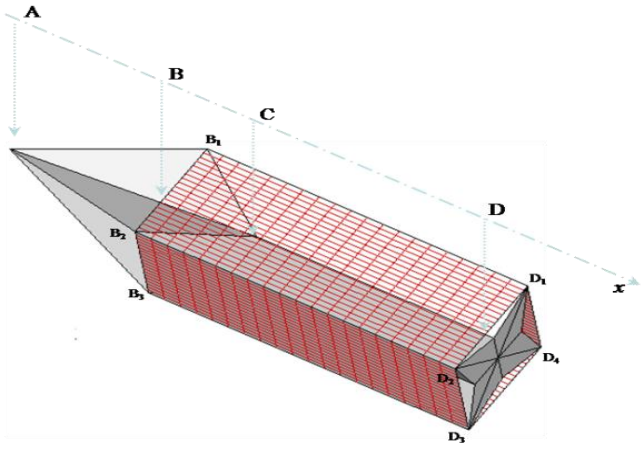

Figure 4.1. A Typical 4-point Star Inlet

Although acquiring the much needed and rich details of the appropriate flowfields, it is important to note that efforts were taken to reduce the computational costs. Therefore, a new strategy is formulated and executed as part of this thesis. This thesis is focused only on the detailed study of a single streamtube that is associated with a typical 4-point star inlet. All computations are conducted on a typical streamtube, as illustrated in Figure 4.2. Furthermore, the studies of interest to this thesis are geared not only towards the evaluation of the flow inside the streamtube, but also the flow captured at the inlet of the streamtube. The execution of this thesis efforts are conducted at two locations, using two sets of CFD Tools, namely, NCAT, WPAB, FLUENT, and AVUS respectively. This chapter describes the computational efforts and the results associated with these studies.

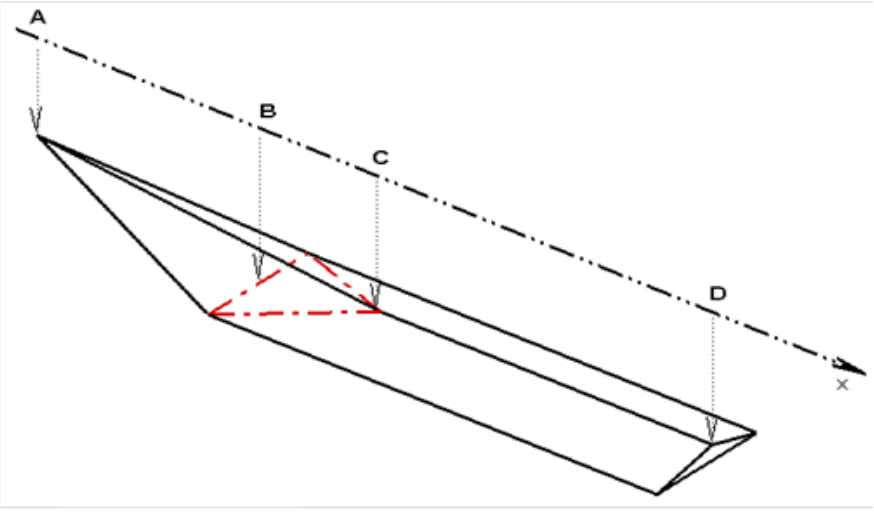

Figure 4.2. A Typical Streamtube Associated with the 4-point Star Inlet

4.1 FLUENT Evaluations

As described earlier, GAMBIT, the grid generation software created by the developers of FLUENT, was used to formulate the geometry of the streamtube of interest and subsequently the grids associate with this geometry. In an effort to evaluate the 4-point star-shaped configuration with as much technical details as possible, the evaluation was conducted in a step by step manner relative to the technical difficulties associated with the CFD models. In the case of the GAMBIT-FLUENT CFD Tool, two evaluations were conducted, namely a 2D and a 3D analysis. GAMBIT is flexible enough to allow for the creation of points, curves, surfaces and finally volumes. This approach is known as the "Bottom-Up" approach to creating a grid. Also, this particular gridding method allows the user to have ultimate control over grid clustering and their placements. The 2D and 3D grids were generated by GAMBIT, and illustrated in Figures 4.3 and 4.4.

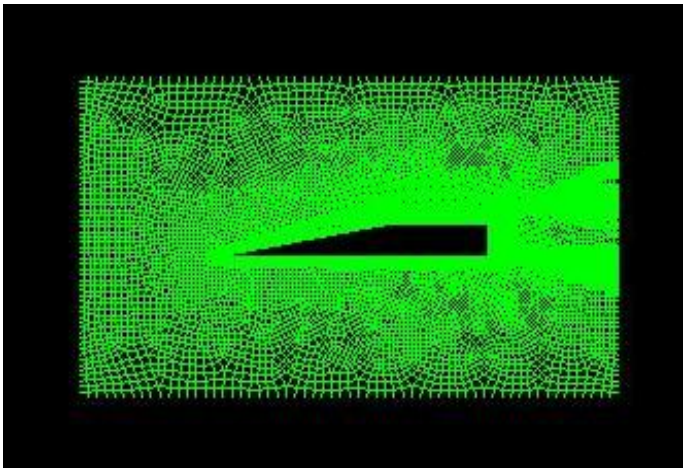

Figure 4.3. 2D Grid of the Streamtube

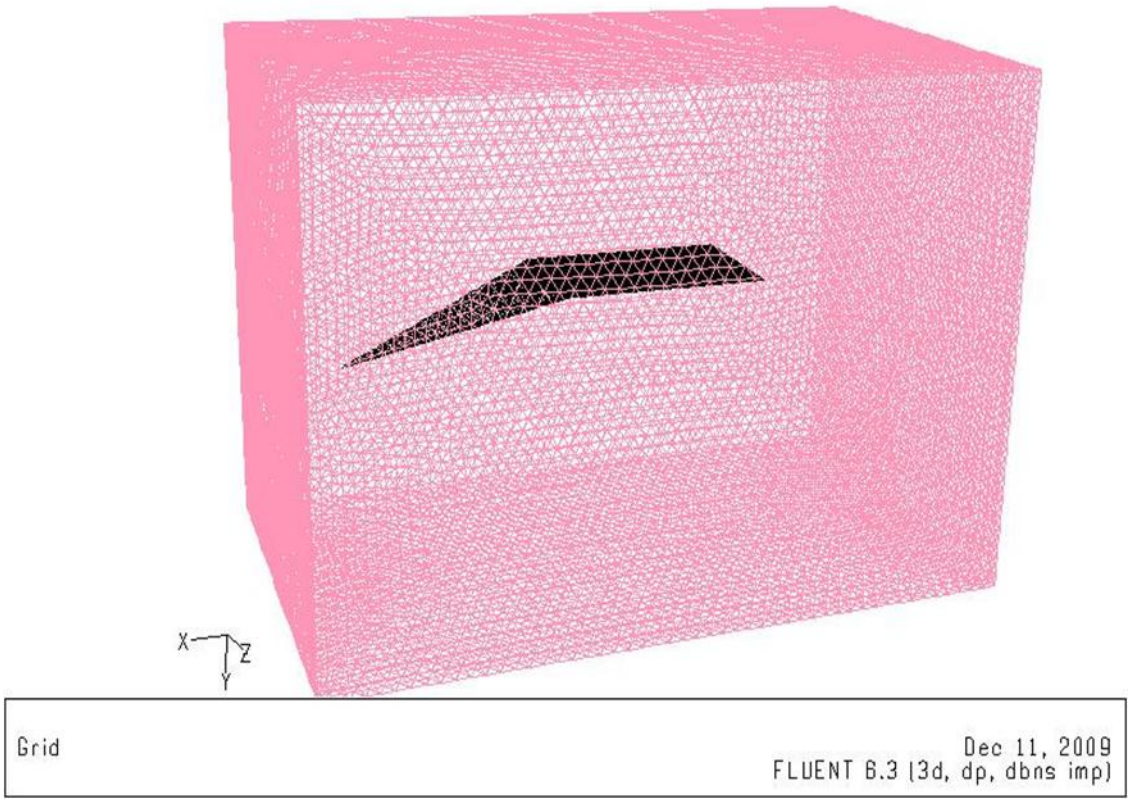

Figure 4.4. 3D Grid of the Streamtube

Once developed, the grid information along the freestream data and CFD model information are assigned and submitted to FLUENT for further flowfield evaluation. In this thesis, the stream tube was evaluated at a freestream mach number of 6.0 at an altitude of 30 km. The 4-point star streamtube was constructed with a wedge angle of 17.5 degrees. In addition, the flowfield was assumed turbulent and the Spalart-Allmaras model was selected in the flowfield evaluation process. The results for the 2D evaluations are described in Figures 4.5 and 4.6 in the form of mach numbers and pressure contours, respectively.

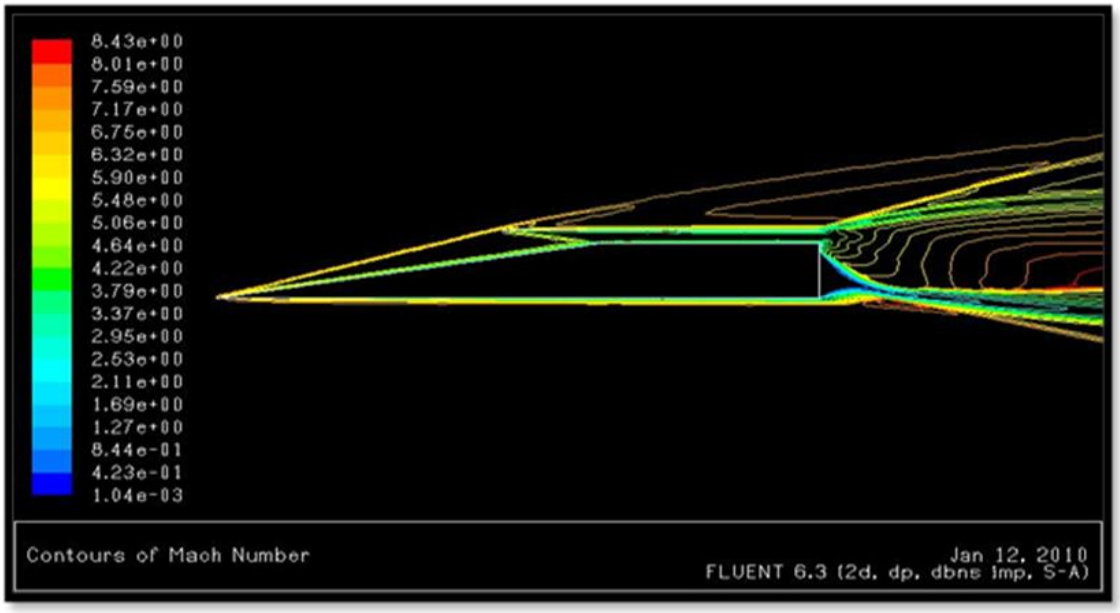

Figure 4.5. Mach 6 Freestream with Contours of Mach Number

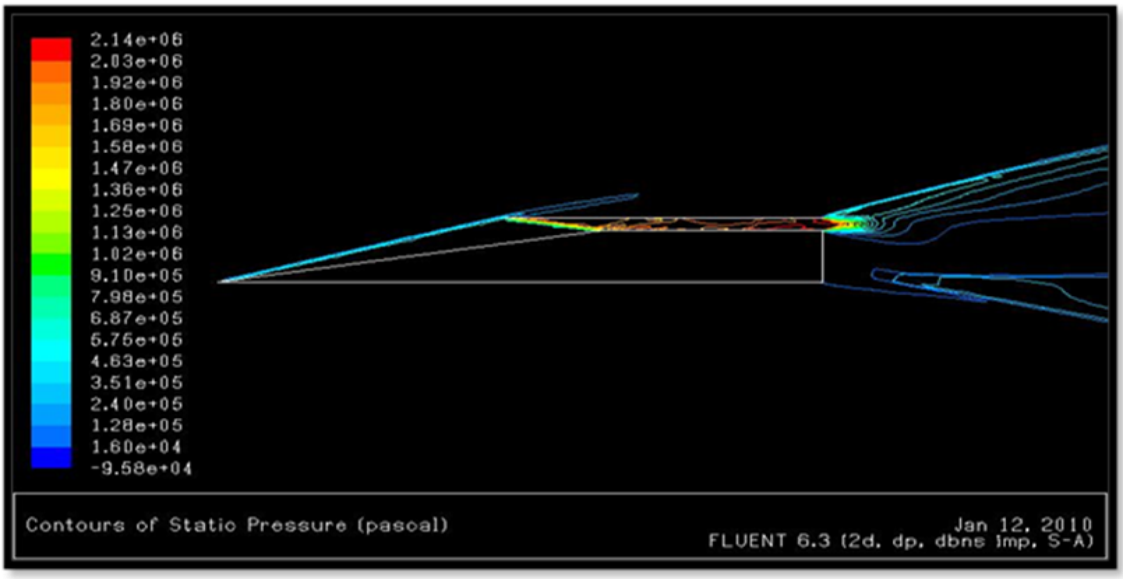

Figure 4.6. Mach 6 Freestream with Contours of Pressure

The results of this 2D evaluation showed that the expected flowfield behaviors are recovered. In both illustrations of Figures 4.5 and 4.6, it can be seen that the primary and reflected shocks are recovered, and the primary flowfield at the inlet is uniform. In Figure 4.5, a concentration of the Mach contour at the boundaries inside the streamtube indicated that boundary layers were developed. In the case of Figure 4.6, a weak shock train can be observed in the isolator. However, a detailed looked at the velocity field indicated that the strength of the shock train is not severe enough to allow for any significant variation of the internal flowfield. It is important to note that the external flowfield associated with the results illustrated in Figures 4.5 and 4.6 are not important to this thesis. The external flow is used mainly to demonstrate that the inlet captures the desired mass flow. Nevertheless, as illustrated in Figures 4.5 and 4.6 the flow around the tube behaves as expected. The results obtained from the 2D evaluations are very encouraging, and suggested that the 2D model of the 4-point star-shaped forebody perform as designed.

Pleased with the 2-D results, a 3-D analysis was conducted with FLUENT. The results of this study are illustrated in Figures 4.7 and 4.8. The results represent the mach number distribution along the centerline geometry of the stream tube and along a fixed x-cross section in of the isolator exit. Obviously, these results are inconclusive and unsatisfactory. No convergence in any of the flowfield variables was obtained.

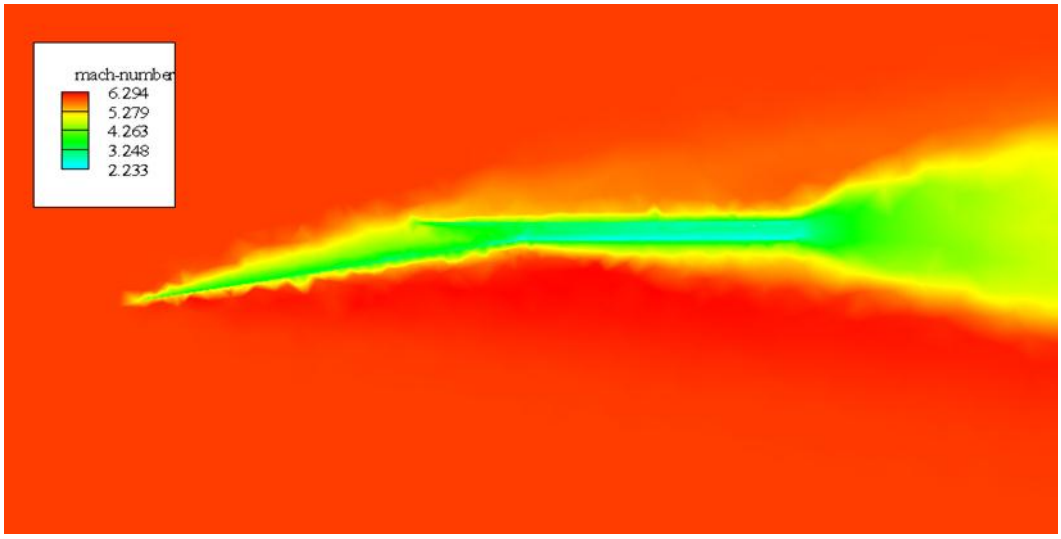

Figure 4.7. 3D Mach 6 Contours of Mach Number, centerline z-axis

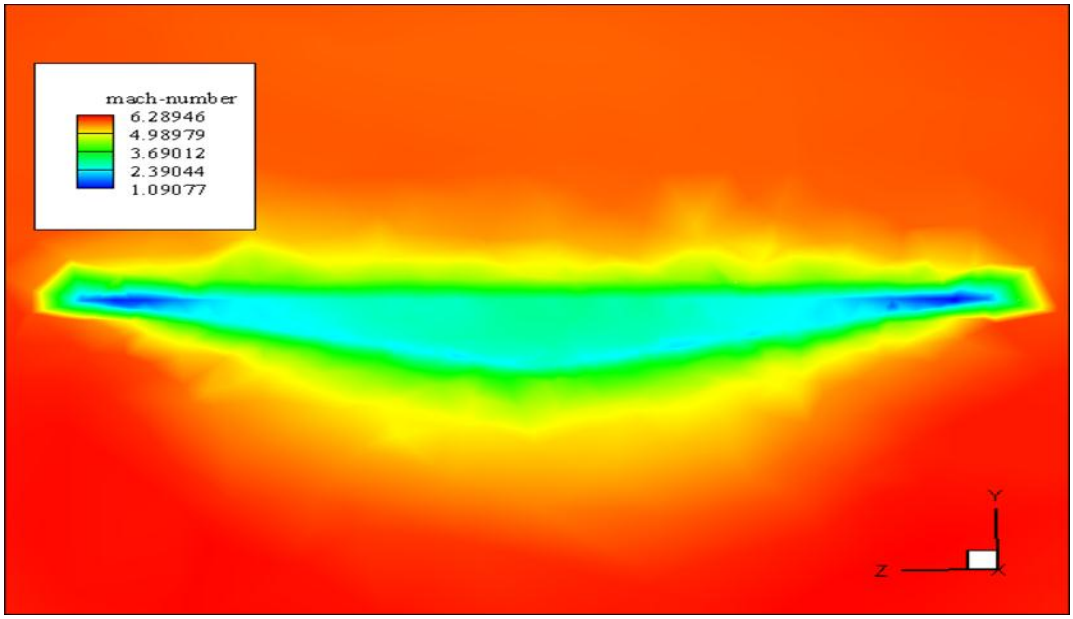

Figure 4.8. 3D Contours of Mach Number, isolator exit

Upon closer examination of Figures 4.7 and 4.8 indicates that it is unclear where the actual streamtube surfaces are established. Specifically, in Figure 4.7, the primary and reflective shocks are ambiguous. These results are a direct result of the grid density, or lack thereof. At NCAT, FLUENT was executed upon a personal computer, where large grid sizes are prohibited due to the limited availability of random access memory, RAM. Results for large grids are capable, but a solution will require a long test time. Since these results were inconclusive, another approach to 3-D results must be explored. The next step in the analysis process is to analyze the streamtube using AVUS.

4.2 AVUS Evaluations

The Gridgen-AVUS combination is the second of two sets of software used as part of the CFD analysis associated with the scramjet forebody flowfield. The grid generation software, Gridgen, was used primarily to produce high quality grids for the AVUS code. Unlike GAMBIT, Gridgen is a software that is designed to be used as a universal grid generator. However, like GAMBIT, Gridgen is a GUI based software that incorporates the "Bottom-up" approach during the grid generation process. Using Gridgen, a set of grids were developed that incorporated 24 layers of prism like cells along the wall boundaries of the streamtubes. The prism cells were very much needed, if the technical details associated with a turbulent boundary layer were to be captured. The smoothing and gradual transformation of the grids from prisms at the surface to rectangular like cells at the center of the duct required great flexibility. Gridgen allows for this flexibility and allows the user numerous opportunities to analyze the quality of the grid prior to

submission to the AVUS solver. Illustration of the 24 prism layers that were incorporated in the unstructured grid used in this analysis are presented in Figures 4.9 and 4.10.

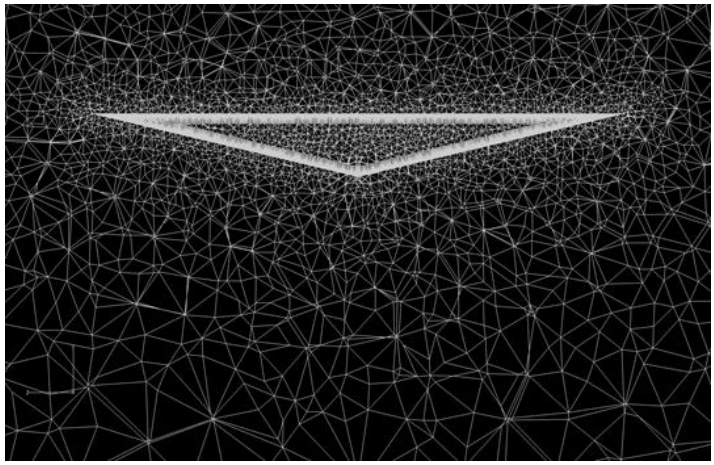

Figure 4.9. 2D X - Cross Sectional Illustration of the Grid Created in Gridgen

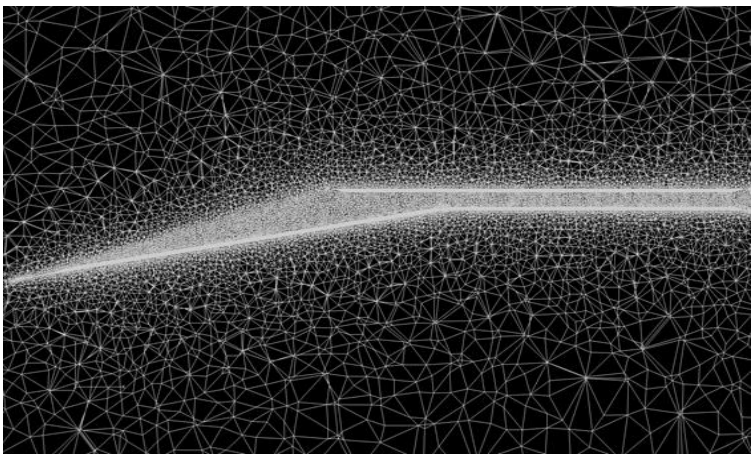

Figure 4.10. 2D Z - Cross Sectional Illustration of the Grid Created in Gridgen

Once developed, the grid information along with the freestream data and CFD model information are assigned and submitted to AVUS for further flowfield evaluation. Recall, in this thesis, the streamtube was evaluated at a freestream mach number of 6.0 at an altitude of 30 km. The 4-point star streamtube was constructed with a wedge angle of 17.5 degrees. In addition the flowfield was assumed turbulent and the Spalart-Almaras model was selected in the flowfield evaluation process.

Unfortunately, after numerous attempts, the results for the 3D viscous analysis evaluations were inconclusive as seen in Figure 4.7. Even though the grids were refined and modified numerous times, no credible viscous results were obtained. As such no credible viscous results will be presented. However, Euler results were obtained. Moreover, the Euler results support the inverse design concept that was used to construct the scramjet forebody. The 3D Euler results are presented in Figures 4.11 – 4.17 in the form of 2D data slices. In Figure 4.18 the 2D data slices are arranged in manner that illustrates their relative location as they support the scramjet forebody internal flowfield. Figures 4.11 and 4.12 illustrate 2D slices of the forebody inlet mach number and pressure distribution along the centerline plane of scramjet inlet. As noted in Figure 4.11, the mach number distribution between the primary and reflected shock waves is uniform. Also, there only are minor variations in the isolator region. This information is as expected. In Figure 4.12 the pressure distribution between the primary and reflected shock waves, however, there is distinct evidence of an oblique shock train in the isolator. A closer look at this result indicates that even though there are reflected shock waves in the isolator, these shock waves are weak, and they do not contribute to the realignment of

the velocity flow field. The 2D data slices taken at the entrance and exit of the isolator in planes normal to the x-axis confirm these findings. Refer to the mach number contour plots given in Figures 4.13 and 4.14.

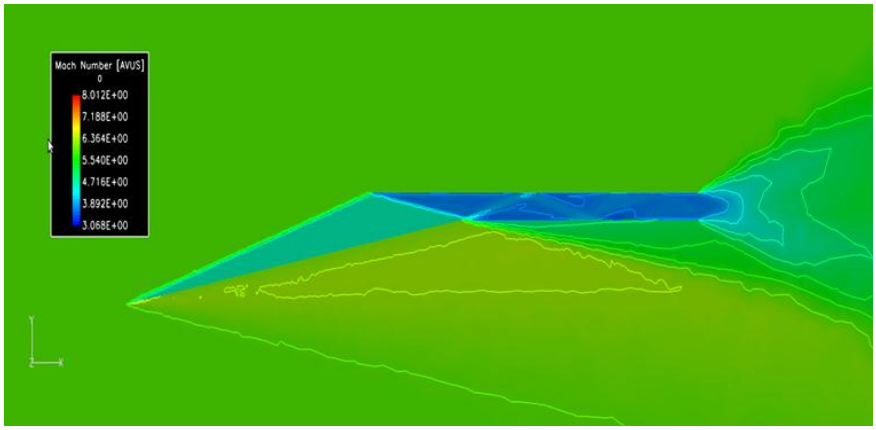

Figure 4.11. 3D Contours of Mach Number, centerline z-axis

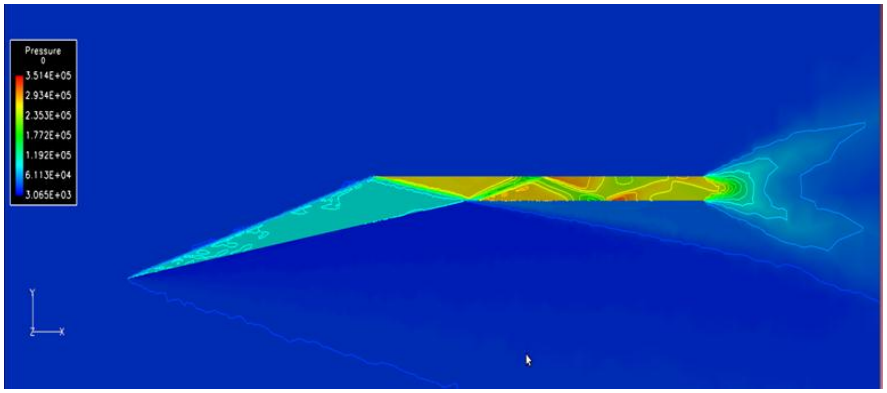

Figure 4.12. 3D Contours of Pressure, centerline z-axis

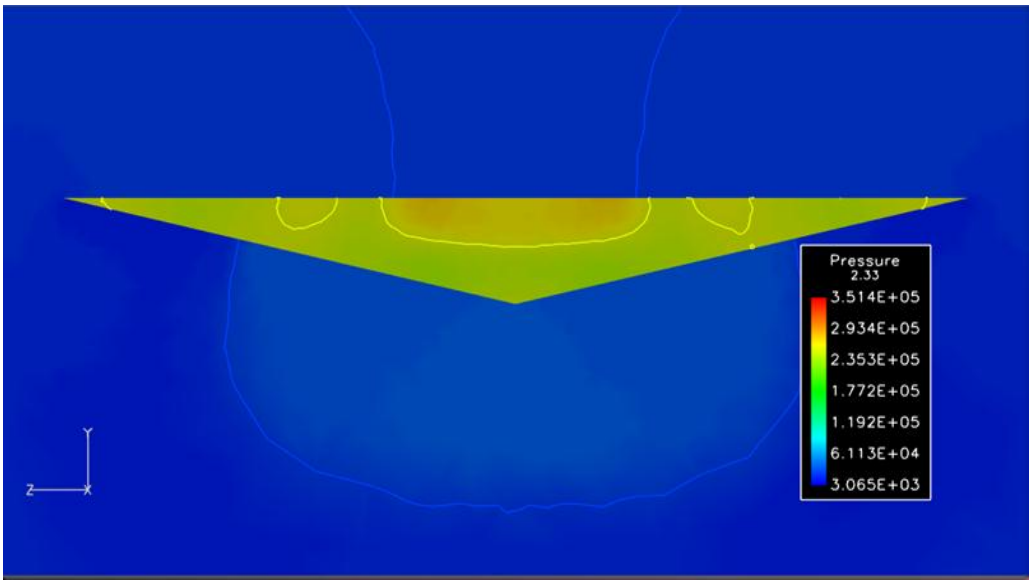

Figure 4.13. 3D Mach 6 Contours of Pressure, isolator exit

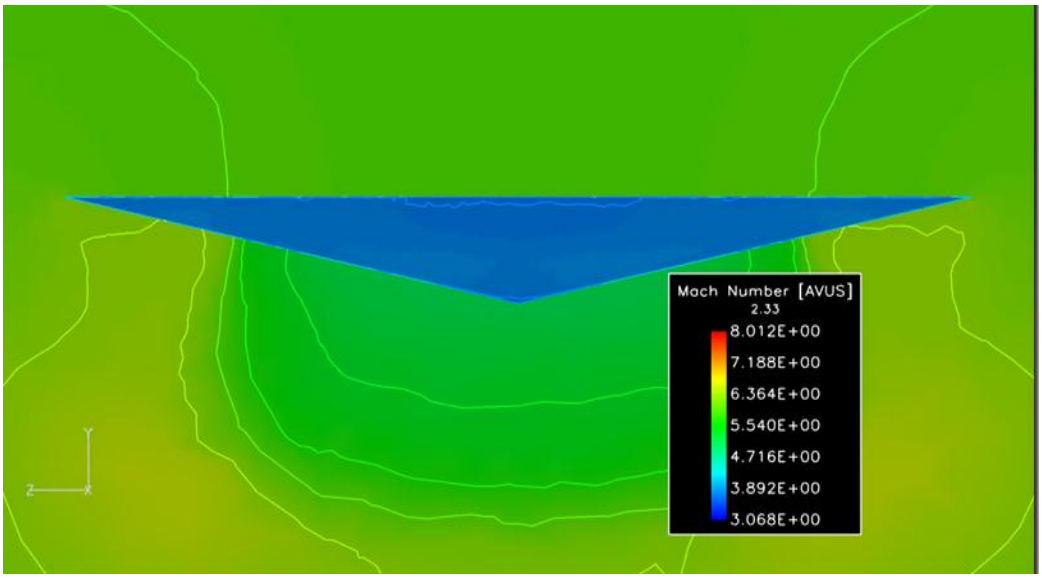

Figure 4.14. 3D Mach 6 Contours of Mach Number, isolator exit

In a similar manner, the Euler results of the 3D flow field studies were presented in 2D slices with normals in the y-axis. Samples of the mach number and pressure distributions at the center of the isolator relative to its height are illustrated in Figures 4. 15 and 4.16. As illustrated earlier, the Mach number plots showed very weak waves and little flow disturbances. The pressure plots, however, showed the reflected weak shock train but no significant disturbances in the velocity fields. Also illustrated in Figures 4.15 and 4.16 the mach number and pressure contours indicated that as the flow approaches the exit of the isolator the Mach number and pressure become uniform. This is the quality of flow that is required by the scramjet and the conditions for which the isolator was designed.

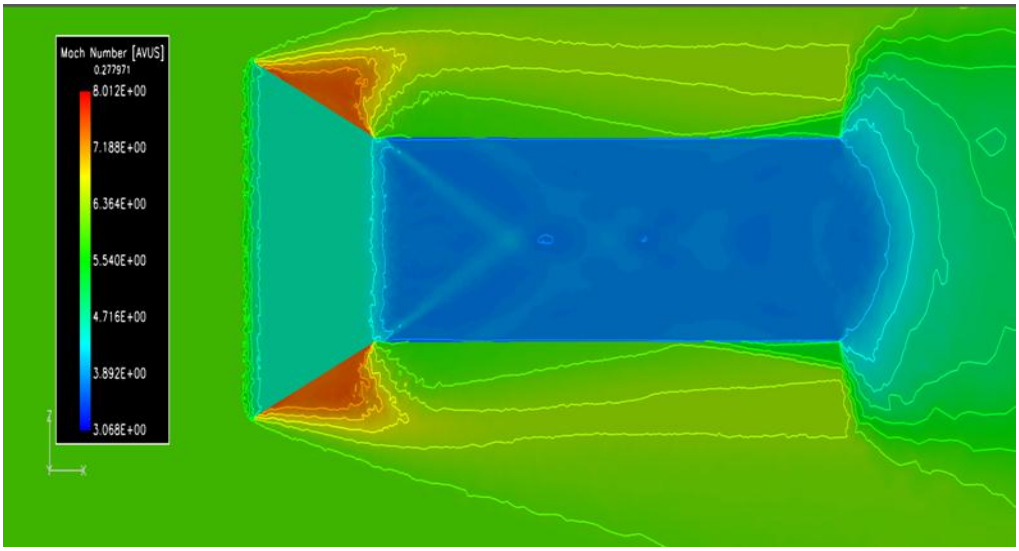

Figure 4.15. 3D Mach 6 Contours of Mach Number, centerline y-axis

In an effort to demonstrate that the internal flowfield within the scramjet forebody is truly 2D in nature, contours plots of the w-components of the velocity vector were developed. A sample of the w-components of the velocity vector is illustrated in Figure 4.17. This result indicates that there are no movements in the z-directions, and confirms that the flowfield is truly two-dimensional. Finally, Figure 4.18 represents the 2D data slices that are arranged in a manner that illustrates their relative location as they support the scramjet forebody internal flowfield.

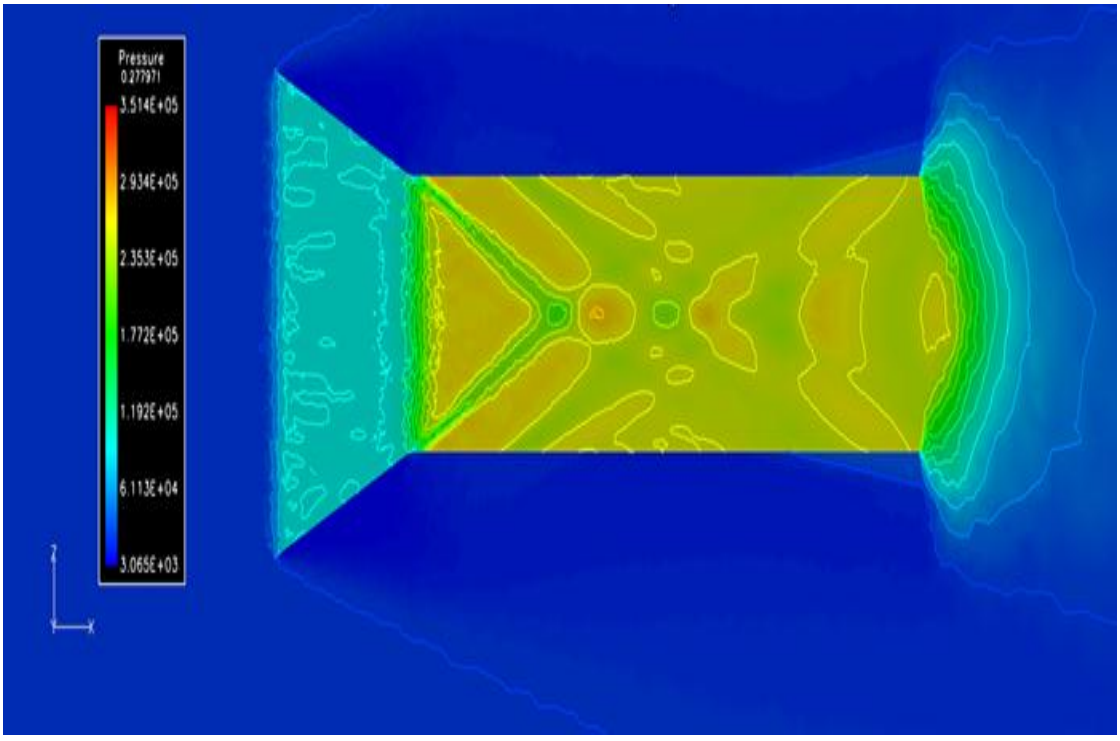

Figure 4.16. 3D Mach 6 Contours of Pressure, centerline y-axis

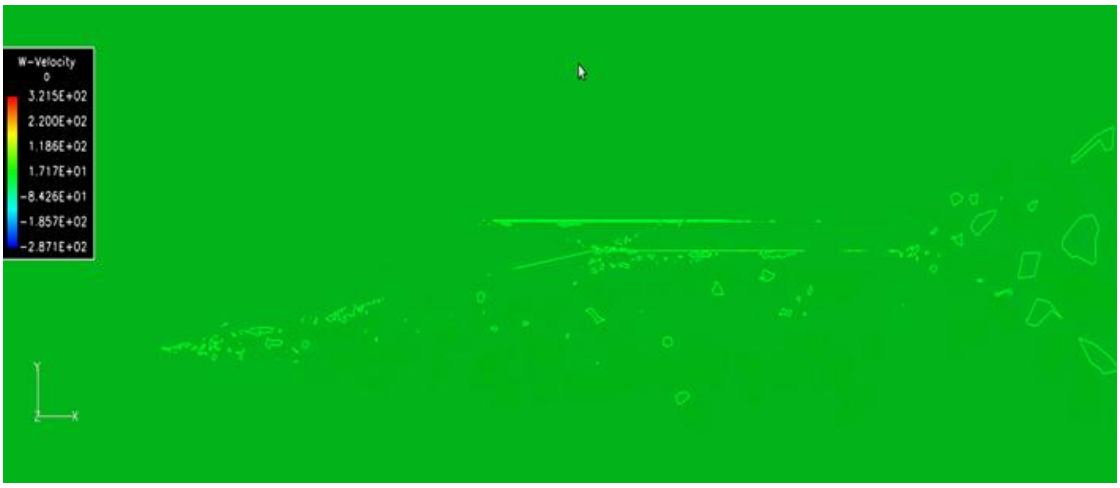

Figure 4.17. 3D Mach 6 Contours of Z-Component of Velocity, centerline z-axis

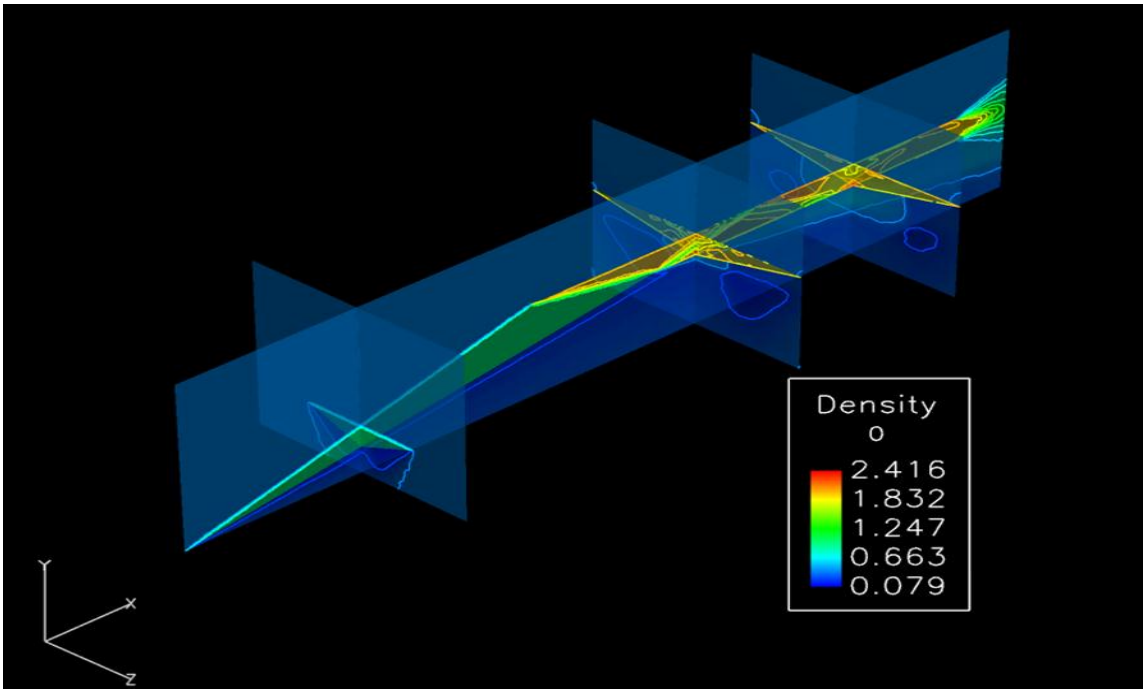

Figure 4.18. Flow Visualization Demonstration, Mach 6: Contours of Density

4.3 Validation of Results

It is good practice to validate all results obtained from CFD studies. The validation process is usually done through the use of a comparative process. Typically, the CFD data is measured against available experimental results or other independently obtained computational results of the same problem. Currently, there are no known experimental data of the flowfield studied herein. There is however, a similar CFD study that was carried out by a colleague (Ferguson, 2009), Nastassja Dasque, in 2008. In her study, Dasque conducted a Mach 5 inviscid analysis of the complete four-point-star configuration. The results from the analysis are presented in Figures 4.19 (Ferguson, 2009)and 4.20 (Ferguson, 2009). A detailed description of this analysis can be found in (Ferguson, 2009).

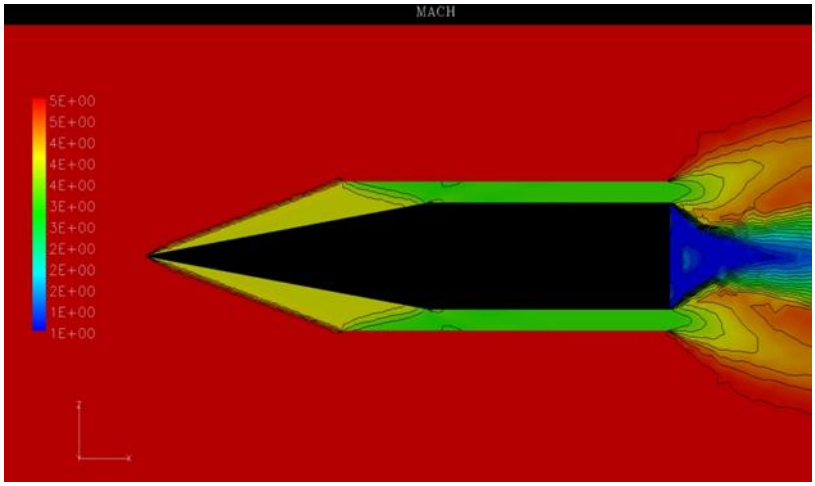

Figure 4.19. Independent Validation; Contours of Mach Number

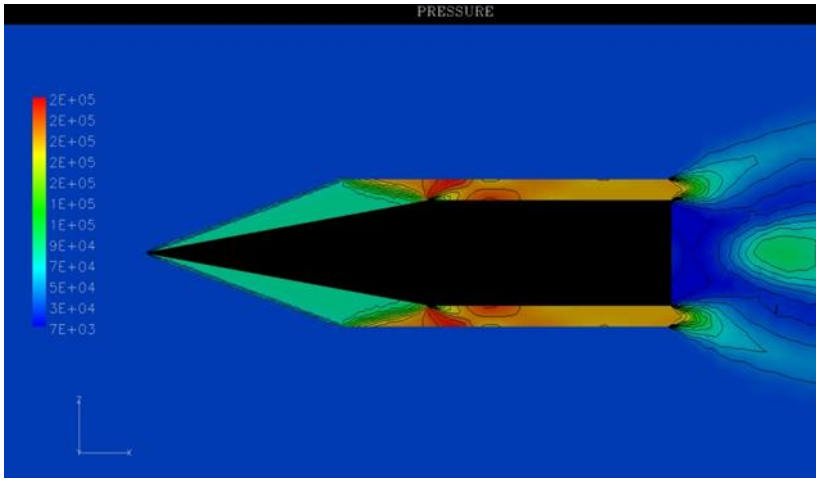

Figure 4.20. Independent Validation; Contours of Pressure

The results indicated in Figures 4.18 and 4.19 bear a striking resemblance to the results generated by this study, as seen in Figures 4.11 and 4.12. Both sets of results recover the primary and reflective oblique shock waves. Also, there are no strong oblique or normal shock waves in the isolator. Although these two sets of data bear a strong resemblance to each other, there is a major difference that points to one fact. Dasque results do not recover the oblique shock train in the isolator. This is due to the simple fact that she modeled all four stream tubes in her analysis. A consequence of this choice reduces the number of grid points in the isolator available to capture minute disturbances in the flowfield.

CHAPTER 5

CONCLUSION

A four-point-star mach 6.0 configuration was independently tested using two Navier-Stokes Solvers. FLUENTTM was first utilized to conduct the analysis of interest to this thesis at North Carolina Agricultural and Technical State University. AVUS was also utilized to conduct the analysis of interest to this thesis at the Air Force Research Laboratory. This analysis was initiated with a 2-D viscous study. After concluding that the 2D results were promising and very satisfactory, a more intensive 3D analysis was conducted. The results of the 3D analysis were inconclusive, but not entirely fruitless. The FLUENT 3D viscous analysis revealed that a highly dense grid was necessary to capture the true physics of the complex flowfield.

Shifting the analysis toward AVUS, this goal was accomplished. Associated with moving to a new Navier-Stokes Solver, new grids were produced using GridgenTM. Results from the Euler analysis performed in AVUS were very promising. As described in this thesis, recovering of the 2D flowfield is revolutionary in the field of hypersonics. Although the results are very promising, there is still more work to be done in this effort. Efforts are underway to conduct a 3D viscous analysis with a higher fidelity model in AVUS. Once this task is complete, the analysis efforts should shift to analyzing Phase II of the design process.

REFERENCES

Air Force Research Laboratory, (2007). *Air Vehicles Unstructured solver User's Manual*, Wright Patterson Air Force Base, OH.

Akbarzada, M., & Kermani, M.J.,(2007). *Numerical Computation of Supersonic-subsonic Ramjet Inlets; a Design Procedure*, ISME2007-3056.

Alexandrov, N. M., *Using Variable-Fidelity Models in Multidisciplinary Design Optimization*. Retrieved August 24, 2010, from http://fmad-www.larc.nasa.gov/mdob/users/natalia/approximations

Anderson, J. D. (2001). *Fundamentals of Aerodynamics* Third Edition, McGraw-Hill, New York.

Andreadis, D., (1996). *Scramjet Engines Enabling The Seamless Integration Of Air & Space Operations*, Pratt & Whitney Space Propulsion, Hartford, CT.

Ansari, A. & Strang, W. Z., (1996). *Large-Eddy Simulation of Turbulent Mixing Layers*, AIAA-96-0684.

Atkinson, Michael D.,(2007). *Numerical Investigation of A Super-Sonic Inlet Using Bleed and Micro-Ramps to control Shock-Wave/Boundary Layer Interactions*, AIAA Paper 2007-24.

Apdin, H., & Ferguson, F. , (2005). *A Design Concept for the Construction of Completed Hypersonic Vehicles*, 13th AIAA/CIRA International Space Planes and Hypersonic Systems and Technologies Conference, CIRCA, Italy.

Balakrishnan, L. & Sarkar, S.,(1990). *Application of a Reynolds-Stress Turbulence Model to the Compressible Shear Layer*, ICASE Report 90-18, NASA CR 182002.

Billig F. S.; (1993). *Research on Supersonic Combustion,* Journal of Propulsion and Power, Vol. 9, No 4.

Borger, W., (2005). *Disruptive Technology: Hypersonic Propulsion*, Technical Brief, Propulsion Directorate-Air Force Research Laboratory, AFRL HQ 07-0083, Wright-Patterson Air Force Base, OH.

Bowcutt, K. G., (1986). *Optimization of hypersonic Waveriders Derived from Cone Flows Including Viscous Effects*, Ph.D. Dissertation, Department of Aerospace Engineering, University of Maryland, College Park, Maryland.

Bowcutt, K. G., Anderson, J. D. Jr., & Capriotti, D.P., (1987). *Viscous Optimized Hypersonic Waveriders*, AIAA paper 87-0272.

Clarke, D.B., & Jones, D.A., (2005). *Simulation of a Wing-Body Junction Experiment using the Fluent Code,* Australian Government; Department of Defense: Defense Science and Technology Organization, DSTO-TR-1731, Fishermans Bend, Victoria 3207 Australia.

Constantinescu, G. S., & Squires, K. D., (2000). *LES and DES Investigations of Turbulent Flow over a Sphere,* AIAA 00-0540.

Curran, E. T,. & S.N.B. Murthy, (2000). *Scramjet Propulsion*, Vol. 189, AIAA.

Dhanasar, M.,(2005). *A Method for the Design and Analysis of Deep Space Nuclear Propulsion Systems*, Master's Thesis, Department of Chemical and Mechanical Engineering, North Carolina Agricultural and Technical State University, Greensboro,NC.

Dhanasar, M., (2009). *Development of a Benchmark Model for the Design and Analysis of a Tip-To-Tail Ramjet–Scramjet Propulsion System*, Ph. D Dissertation, Department of Mechanical Engineering, North Carolina Agricultural and Technical State University, Greensboro, NC.

Elamin, G., (2008). *THE INTEGRAL-DIFFERENTIAL SCHEME(IDS): A NEW CFD SOLVER FOR THE SYSTEM OF THE NAVIER-STOKES EQUATIONS WITH APPLICATIONS*, Ph. D Dissertation, Department of Mechanical Engineering, North Carolina Agricultural and Technical State University, Greensboro,NC.

Ferguson, F., (1993). *Expanding the Waverider Design Space Using Arbitrary Generating Flowfields*, Ph.D. Dissertation, Department of Aerospace Engineering, University of Maryland, College Park, Maryland.

Ferguson, F., Corbett, T. L., Akwaboa, S., & Lindsay, H., (2007). *The Development of Waveriders From an Axisymmetric Flowfield*, AIAA 2007-847, 45th American Institute of Aeronautics and Astronautics Aerospace Sciences Meeting and Exhibit, Reno, NV.

Ferguson, F., Dhanasar, M., Williams, R., Blankson , I., & Kankam, D. (2008). Supersonic and Hypersonic Air-Breathing Configurations Derived from 2D Flowfields, AIAA-2008-163, 46th American Institute of Aeronautics and Astronautics Aerospace Sciences Meeting and Exhibit, Reno, NV.

Ferguson, F., Dhanasar, M., & Blankson , I. (2009). Preliminary Design of a Tip-to-Tail Model of a Ram-Scram Jet Engine, AIAA-2009-714, 47th American Institute of Aeronautics and Astronautics Aerospace Sciences Meeting and Exhibit, Orlando, FL.

Ferguson, F., Fiagbe , Y., & Dasque, N. (2009). Design of Optimized 3D Tip-to-tail Scramjet Engines, AIAA-2009-1099, 47th American Institute of Aeronautics and Astronautics Aerospace Sciences Meeting and Exhibit, Orlando, FL.

FLUENT, Retrieved September 15, 2010, from http://my.fit.edu/itresources/manuals/fluent6.3/help/html/ug/node461.htm

Godunov, S. K.;(1959). *A Finite Difference Method for the Numerical Calculation of Discontinuous Solutions of the Equations of Fluid Dynamics*. Mat. Sb., Vol 47, pp 271-290.

Goldsmith E.L., Sedona J., (1999). *Intake Aerodynamics*, Blackwell Science, Second Edition.

Gossiping P., & Lesage F., Champlain Aide., "The Application of Computational Fluid Dynamics (CFD) For the Design of Rectangular Supersonic Intakes", *Proceedings of CFD 98 Conference.* 1998.

Gottlieb, J. J. & Groth, C. P. T.,(1988). *Assessment of Riemann Solvers for Unsteady One-Dimensional Inviscid Flows of Perfect Gases*. J. Comp. Phys., Vol 78, pp 437-458.

Hallion, R. P., (2005). *The History of Hypersonics: or, Back to the Future – Again and again*, AIAA Paper 2005-0329.

Heiser, W. H., & Pratt, D. T. (1994) *Hypersonic Airbreathing Propulsion*, AIAA Education Series. ISBN: 1-56347-035-7, Published by American Institute of Aeronautics and Astronautics.

Issa, R.I., Gosman, A.D., & Watkins, A.P., (1986). *The Computation of Compressible and Incompressible Recirculating Flows, J. Comput. Phys.*, 62, pp. 66-82.

Karypis, G. & Kumar, V., (1995). *METIS Unstructured Graph Partitioning and Sparse Matrix Ordering System Version 2.0,* Dept. of Computer Science, Univ. of Minnesota.

Kennon, S. R., Meyering, J. M., Berry, C. W., & Oden, J. T., (1992). *Geometry Based Delaunay Tetrahedralization and Mesh Movement Strategies for Multi-Body CFD,* AIAA-92-4575.

Lindsay, H. , Ferguson, F., Akwaboa, S. , & Apdin, H., (2006). *The Construction of Integrated Hypersonic Vehicles from 2D Flowfields,* 42nd AIAA/ASME/SAE/ASEE Joint Propulsion Conference & Exhibit.

MacCormack, R. W., (1969). *The Effect of Viscosity in Hypervelocity Impact Cratering,* AIAA-69-0354.

Menter, F. R., Zonal, (1993). *Two Equation k-ω Turbulence Models for Aerodynamic Flows,* AIAA 93-2906.

Montgomerie, B.; & Hasselrot, A., (2005). *An Overview of Propulsion Systems for Flying Vehicles,* Swedish Defense Research Agency, FOI-R-1563-SE.

Parikh, P., Pirzadeh, S., & Frink, N. T., (1992). *Unstructured Grid Solutions to a Wing/Pylon/Store Configuration Using VGRID3D/USM3D,* AIAA-92-4572.

Patankar, S.V., & Spalding, D.B., (2007). *A Calculation Procedure for Heat, Mass and Momentum Transfer in Three-Dimensional Parabolic Flows, Int. J. Heat Mass Transfer*", 15, 1787.

Pope, S. B., (2000). *Turbulent Flows,* Cambridge University Press.

Riff, C., (2004). *Computational Fluid Dynamics (CFD) Modeling,* Laboratory for Product and Process Design.

Spalart, P. R. & Allmaras, S. R., (1992). *A One-Equation Turbulence Model for Aerodynamic Flows,* AIAA-92-0439.

Spalart, P.R., Jou, W-H., Strelets, M., & Allmaras, S. R., (1997). *Comments on the Feasibility of LES for Wings, and on a Hybrid RANS/LES Approach*, Advances in DNS/LES, 1st AFOSR Int. Conf. On DNS/LES, Greyden Press, Columbus OH.

Tomaro, R. F., Strang, W. Z., & Sankar, L. N., (1997). *An Implicit Algorithm for Solving Time Dependent Flows on Unstructured Grids*. AIAA-97-0333.

van Doormal, J.P., & Raithby, G.D. (1984). *Enhancements of the SIMPLE Method for Predicting Incompressible Fluid Flows,* Numer. Heat Transfer, 7, pp. 147-163.

van Leer, B.; (1979). *Towards the Ultimate Conservative Difference Scheme. V. A Second-Order Sequel to Godunov's Method,* J. Comp. Phys., Vol 32, pp 101-136.

Waltrup, P. J., & Billig, F. S., (1973). *Prediction of Recompression Wall Pressure Distributions in Scramjet Engines*, Journal of Spacecraft and Rockets, Vol., 10, No. 9, pp. 620-622.

Wikipedia, Retrieved March 16, 2010, from http://en.wikipedia.org/wiki/File:Turboprop_operation-en.svg

Wikipedia, Retrieved March 16, 2010, from http://en.wikipedia.org/wiki/Turbofan

Wikipedia, Retrieved March 16, 2010, from http://en.wikipedia.org/wiki/File:Jet_engine.svg

Wikipedia, Retrieved March 16, 2010, from http://en.wikipedia.org/wiki/File:Ramjet_operation.svg

Wikipedia, Retrieved March 16, 2010, from http://en.wikipedia.org/wiki/Boeing_X-51

Wilcox, D. C., (1998). *Turbulence Modeling for CFD*, pub. DCW Industries,Second Edition.

Zhang, J. & Ferguson, F., *Construction and Analysis of Hypersonic Vehicle Configurations*, 13th AIAA/CIRA International Space Planes and Hypersonic Systems and Technologies Conference, CIRCA, Italy.

APPENDIX A

NONWEILER WAVERIDER

A.1 Nonweiler "Caret" Waverider Revisited

Consider a typical Nonweiler's 'caret' waverider as depicted in Figure A.1. The derivation of this 'caret' shaped configuration which resembles an inverted 'V', as depicted in Figure A.1, was constructed from a section of a single planar oblique shock wave, AB3B4. The caret waverider is the perfect example of a 3D configuration that is derived from a 2D flowfield. The construction is done in such a manner that any cross-section of the resulting geometry that is parallel to the flow represents a wedge that supports an oblique shock wave. To this end, consider any cross-section of the caret waverider that is cut by a xy-plane. Notice how each section resembles a wedge.

In reality, the caret waverider is carved from an inverse design approach that relies on the inviscid streamline principle. The inviscid streamline principle states that any inviscid streamline can be replaced by a solid wall without interfering with the external flow. In addition, since the generating flowfield is an oblique shock wave, the resulting streamlines are represented by straight lines. These streamlines are then pieced together to form planar inviscid stream surfaces. Again, relying on the inviscid flowfield principle, the planar stream surfaces are pieced together to form either 3D waverider configurations or inviscid stream tubes. Again, refer to Figure A.1 and notice how the streamlines form planar stream surfaces, such as, upper inviscid surfaces, ABB_3 and ABB_4, or lower stream surfaces, such as, AB_1B_3 and AB_1B_4. Also, notice how the stream

surfaces are pieced together to form the caret waverider. Constructing a caret shaped waverider, therefore, involves an understanding of the inviscid streamlines and their strict but rigid combination to form inviscid stream surfaces. This concept is explored in the next sub-section.

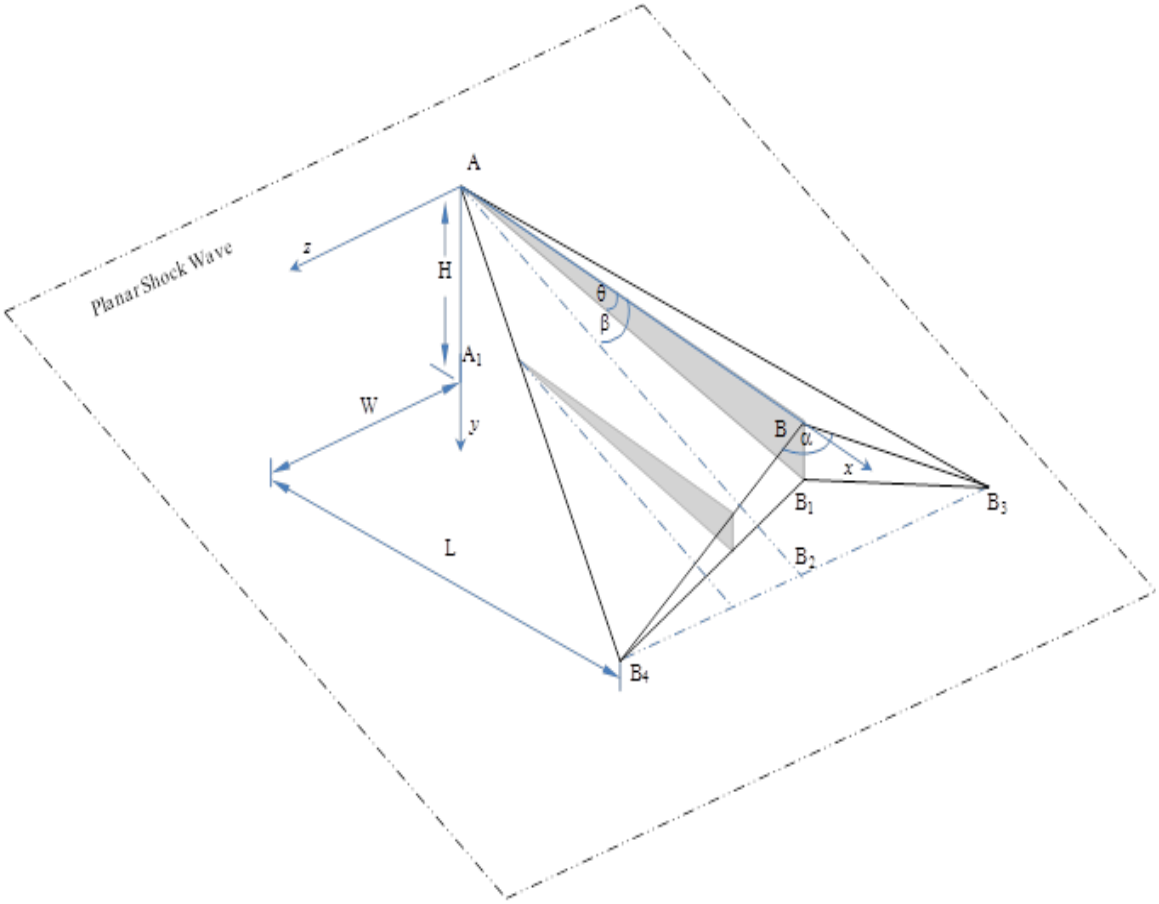

A.1. Nonweiller Caret Wing Waverider Configuration

A.2 3D Forebody Transformation

Consider Figure 2.1 The transformation process starts with one half of the 2D forebody configuration, ABB_1 and the associated flowfield, AB_1B_2, derived from Figure 2.1 and which is now highlighted in Figure A.2. Recall, this flowfield, AB_1B_2, represents a 2D wedge-like flowfield in just a single plane of the 3D scramjet configuration. The challenge is now make an inverse connection, ie., to identify a similar combination of 3D configuration and flowfield structure that locally shares 2D wedge-like flowfields in any one of its cross-sections running parallel to the direction of the flow. This challenge is met through the use of the waverider design concept outlined in the previous section.

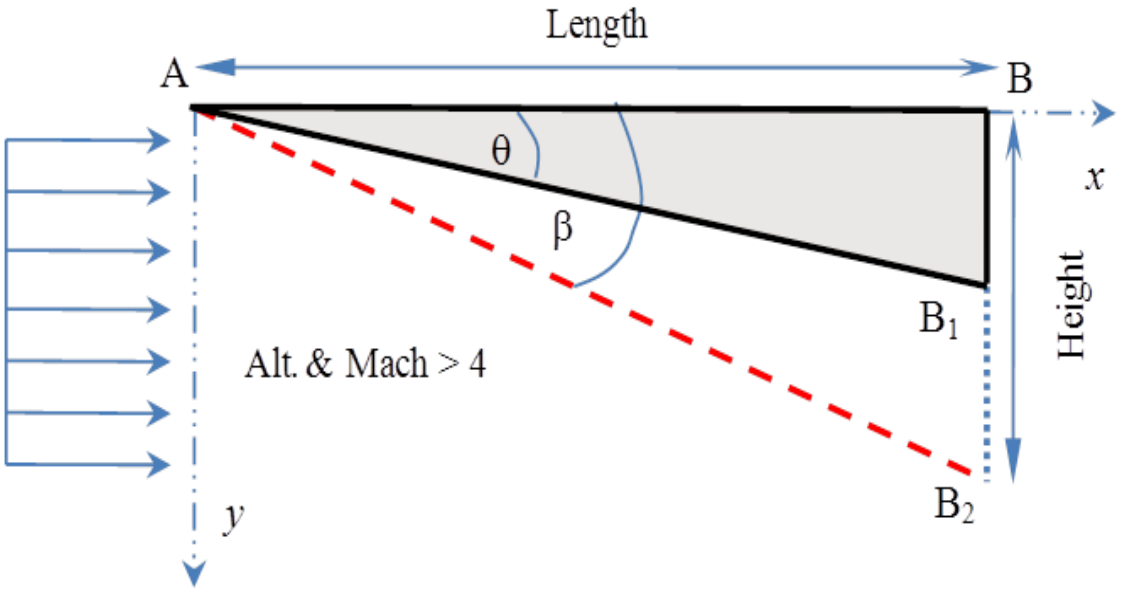

A.2. Illustration of a Wedge-Like Flowfield Segment

Now, consider Figure A.2. Focus on the 2D flowfield and its associated wedge-like geometric cross-section, ABB_1, generated by a xy-plane passing through the center of the caret waverider, refer to Figure A.1. In a similar manner, consider the lower 'one-half' of the 2D Forebody configuration, defined by ABB_1, as illustrated in Figure A.2. Further, compare these two flowfields and their associated wedge-like geometric configurations.

Clearly, the two configurations and their associated flowfields are similar. Moreover, if the generating shock waves are identical, as prescribed by the θ-β-Mach relationships in Equations (2.3 – 2.6), then the 2D configurations and their associated flowfields are identical. In a similar manner it can be shown that the waverider concept is valid for the construction of stream tubes. This concept will be explored later in this section.

A.3 Derivation of Nonweiler 'Caret' Waverider from a Single Shock Wave

The details involve in the construction of the 'caret' waverider start with the definition of two sets of key geometric points, namely Set I and Set II. Set I points are defined as points, such as, A, A_1, B, B_1 and B_2, that are derived in the xy-plane. Set II points are defined as points, such as, B_3 and B_4. These points are defined in the yz-plane and are responsible for the 3rd dimension of the 'caret' waverider. In this analysis, these two sets of geometric points are referred to as the 'waverider design points'. The major objective of the 3D waverider design process is therefore, the definition of these two sets of waverider design points.

Consider 'one-half' of the 2D Forebody configuration, as defined by $ABB_1B_2A_1$. This time focus on the illustrations depicted in Figures 2.1 and A1.1. Figures 2.1 and A.1 represent the centerline cross-section and the base view of the 'caret' waverider. Recall, the Set I points; A, A_1, B, B_1 and B_2, were derived and documented in Section II.A of this paper. As such, the next step in this design analysis is the definition of the Set II points; namely points, B_3 and B_4. As illustrated in Figures 2.8, 2.9 and A1.1, points; B_2, share the same x and y coordinates with points; B_3 and B_4. However, they z components of points; B_3 and B_4 are derived from the expression,

$$B_{3,4}^{z} = \pm B^{y} \tan\left(\frac{\alpha}{2}\right) \tag{12}$$

where the design parameter, angle α, is arbitrarily chosen by the user. In this analysis, the angle α defines the number of star-shaped edges desired at the scramjet inlet. This fact will be made clearer as the analysis progresses. At this stage, the two sets of points; Set I: A, A_1, B, B_1 and B_2, and Set II: B_3 and B_4, are defined. The next step is to construct the stream surfaces.

Once the caret waverider design points are defined, all surfaces and streamlines of importance can be derived. The straight lines representing the leading edges, AB_3 and AB_4, can be defined and constructed. Similarly, planes representing the upper and lower inviscid stream surfaces, such as, upper surfaces, ABB_3 and ABB_4; and lower surfaces, AB_1B_3 and AB_1B_4, can be defined and constructed. The caret configuration derived in Figure 2.8 is composed of the upper stream surfaces, ABB_3 and ABB_4, and the lower stream surfaces, AB_1B_3 and AB_1B_4.

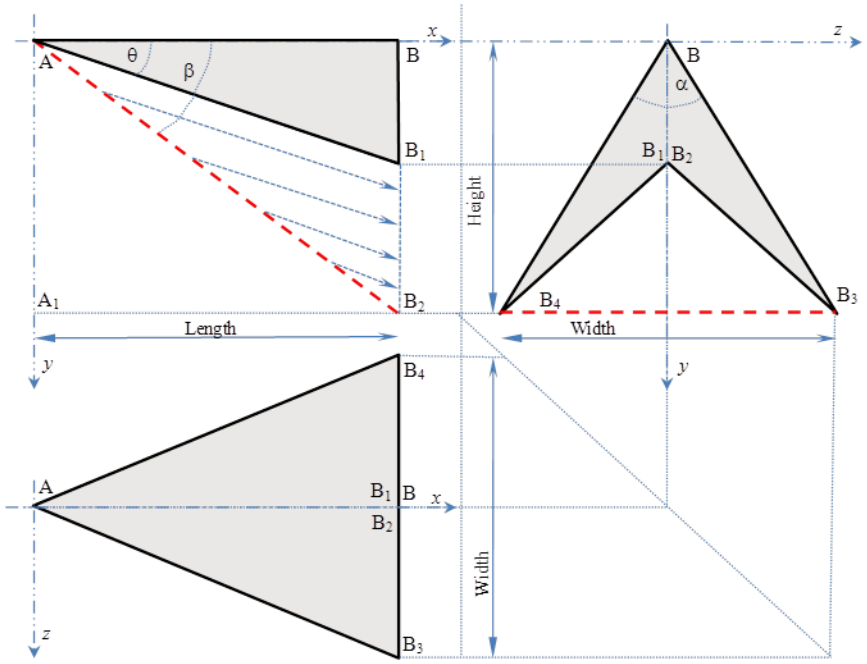

A.3. Caret Waverider Engineering Design Sketches

At this point, it is important to recall the independent points used in the construction of the caret waverider. These are the five caret waverider foundation points; A, B, B_1, B_3, and B_4, with a total of 15 coordinates. In this analysis, these geometric points are referred to as the 'caret waverider design points'. However, even though the 'caret waverider design points' may share some of the same coordinates, they represent a set of 5 independent points that uniquely defines the caret waverider. To illustrate the important connection among the waverider foundation points engineering design sketches of the caret waverider configuration is provided in Figure A.3.

At this stage it is important to recall that the 'waverider design points' are in turn dependent on the five independent design variables, namely, the flight altitude, H, the Mach number, M, the forebody length, L, the wedge angle, θ, and the caret angle, α.

A.4 Derivation od a 4-Point-Star Shaped Configuration

The next step in the design process is to demonstrate that the Nonweiler 'caret' waverder represents only one quarter of the 4-point star-shaped scramjet forebody. When the Nonweiler's approach of inversely carving stream surfaces from inviscid flowfields are extended to multiple shock waves, complete star-shaped configurations can be derived. An illustration of a typical star-shaped configuration that is constructed from a combination of four caret-shaped waveriders is shown in Figure A1.4. The 4-points star-shaped configuration illustrated in Figure 8 is derived from four identical caret-shaped waveriders that were carved from identical flowfields, and pieced together at their common external inviscid stream surfaces. In this case, the caret angle, α, is chosen to be $\pi/2$, such that the resulting configuration forms a closed inviscid stream tube. In a similar manner, the 3- ,4-, 5-, 6- and 8-points star-shaped configurations of interest to this paper are derived. In each case, identical flowfields are used and the caret angle, α, are chosen to be $2\pi/3$, $2\pi/4$, $2\pi/5$, $2\pi/6$, and $2\pi/8$.

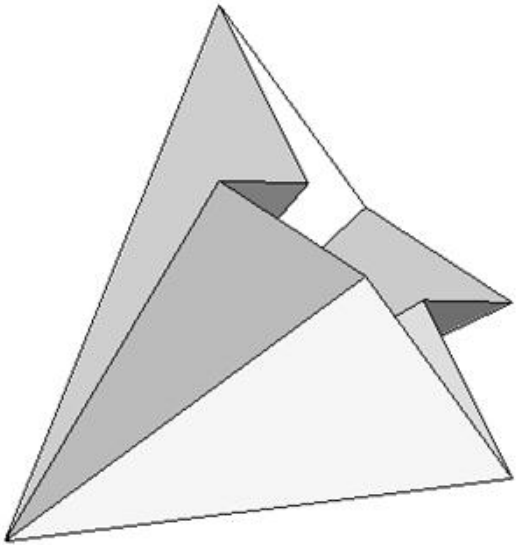

A.4. A Two Caret Combo Waverider

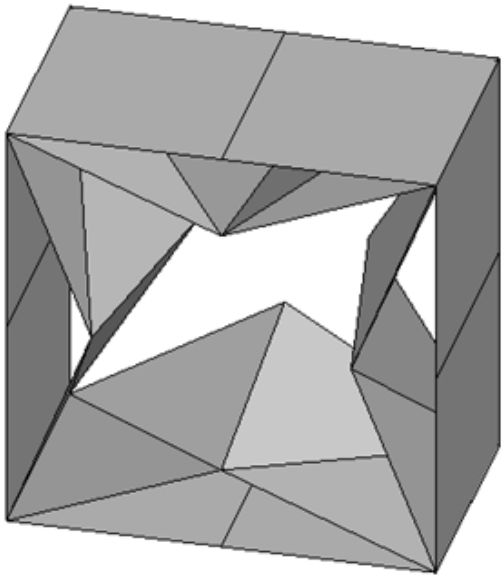

A.5. Four-Points Star-Shaped Inlet

When the waverider concept is used in a similar manner to transform the 2D configuration that shares the two interfaces; namely Station B and Station C, as illustrated in Figure 2.8, the 3D inlet configuration illustrated in Figure A.2 is derived. In like manner, when the 2D configuration that shares the two interfaces; namely Station C and Station D, as illustrated in Figure 2.1, the 3D isolator configuration illustrated in Figure A.3 is derived. Assembling the forebody and inlet designs yields the 4-points star-shaped scramjet forebody configuration depicted in Figure A.4. Using the identical waverider design and assembly principles, the 5- and 6-points star-shaped scramjet forebody configurations depicted in Figures A.5 and A.6 are derived.

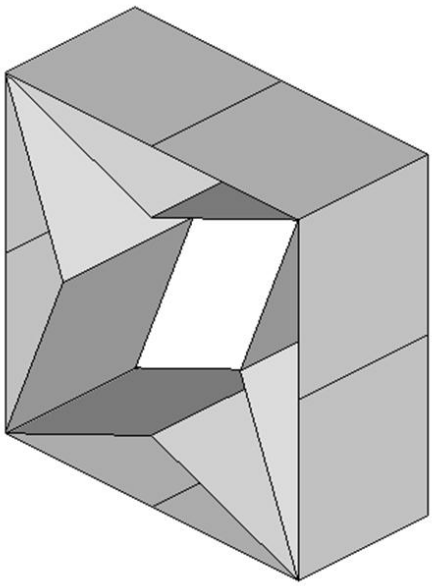

A.6. Four-Points Star-Shaped Isolator

APPENDIX B

FLUENT AND AVUS PROCEDURE

B.1 FLUENT Procedure

The results presented in Chapter 4 were constructed using the following process. All steps taken in this process agree with the FLUENT^{TM} manual.

1) Start the solution by solving the Euler equations and setting the Courrent Number to 0.005.
2) After 10,000 iterations, change the solutions type to a Laminar solution
3) After 10,000 iterations, change the solution type to include the Spalart-Allmaras turbulence model using its default settings.
4) After 10,000 iterations, increase the Courant Number to 0.01
5) Finally, ramp the Courant Number to 25 within 100,000 iterations (0.005,0.01, 0.05, 0.1, 0.5, 1, 5, 10, 15, 25)

B.2 AVUS Procedure

There was not a suggested procedure to use in AVUS. Working closely with its developers, a generic procedure was established that takes the following form.

1) Initialize the solution by setting the CFL number to 0.05 and the dampening coefficients 0.6.
2) After 10,000 iterations, raise the CFL number to 0.1
3) After 5,000 iterations, raise the CFL number to 0.5

4) After 5,000 iterations, raise the CFL number to 0.75
5) After 5,000 iterations, raise the CFL number to 1
6) After 5,000 iterations, raise the CFL number to 5
7) After 5,000 iterations, raise the CFL number to 10
8) After 5,000 iterations, raise the CFL number to 20
9) Finally, lower the dampening coefficients by 0.1 until both coefficients are 0.1 every 5,000 iterations.